

Measurement-and Feedback-Driven Non-Equilibrium Phase Transitions on a Quantum Processor

Zhiyi Wu,^{1,2} Xuandong Sun,^{2,3} Songlei Wang,¹ Jiawei Zhang,^{2,3} Xiaohan Yang,^{2,3} Ji Chu,² Jingjing Niu,^{2,4} Youpeng Zhong,^{2,4,*} Xiao Chen,^{5,†} Zhi-Cheng Yang,^{1,6,‡} and Dapeng Yu^{1,2,4}

¹*School of Physics, Peking University, Beijing 100871, China*

²*International Quantum Academy, Shenzhen 518048, China*

³*Guangdong Provincial Key Laboratory of Quantum Science and Engineering, Southern University of Science and Technology, Shenzhen 518055, China*

⁴*Shenzhen Branch, Hefei National Laboratory, Shenzhen 518048, China*

⁵*Department of Physics, Boston College, Chestnut Hill, MA 02467, USA*

⁶*Center for High Energy Physics, Peking University, Beijing 100871, China*

(Dated: December 10, 2025)

Mid-circuit measurements and feedback operations conditioned on the measurement outcomes are essential for implementing quantum error-correction on quantum hardware. When integrated in quantum many-body dynamics, they can give rise to novel non-equilibrium phase transitions both at the level of each individual quantum trajectory and the averaged quantum channel. Experimentally resolving both transitions on realistic devices has been challenging due to limitations on the fidelity and the significant latency for performing mid-circuit measurements and feedback operations in real time. Here, we develop a superconducting quantum processor that enables global mid-circuit measurement with an average quantum non-demolition (QND) fidelity of 98.7% and fast conditional feedback with a 200 ns real-time decision latency. Using this platform, we demonstrate the coexistence of an absorbing-state transition in the quantum channel and a measurement-induced entanglement transition at the level of individual quantum trajectories. For the absorbing-state transition, we experimentally extract a set of critical exponents at the transition point, which is in excellent agreement with the directed percolation universality class. Crucially, the two transitions occur at distinct values of the tuning parameter. Our results demonstrate that adaptive quantum circuits provide a powerful platform for exploring non-equilibrium quantum many-body dynamics.

I. INTRODUCTION

The past two decades have witnessed remarkable progress in understanding non-equilibrium quantum many-body dynamics. Quantum circuit models [1], originally inspired by quantum computation and quantum algorithms, have proved to be a powerful theoretical framework for exploring universality in non-equilibrium phenomena, such as entanglement growth [2, 3], quantum information scrambling [4–6], and the emergence of hydrodynamic transport [4, 5, 7–9]. Quantum circuit evolutions are also naturally implementable on a variety of gate-based quantum computation and simulation platforms, including superconducting quantum processors, Rydberg atom arrays, and trapped ion systems [10–13].

Quantum hardware, however, offers capabilities that go beyond purely unitary evolution. For example, mid-circuit measurements and feedback operations conditioned on the measurement outcomes are key ingredients for implementing quantum error-correction on quantum devices [14–19]. Moreover, adaptive quantum circuits have been shown to enable more efficient quantum state preparation and the execution of certain quantum algorithms [20–24]. Motivated by the capability of per-

forming mid-circuit measurements experimentally, hybrid quantum circuits where unitary evolutions are interspersed with repeated local measurements have recently attracted interests. Via large-scale numerical simulations and analytically tractable statistical mechanical mappings, it has been demonstrated that by tuning the rate p of mid-circuit measurements, such monitored quantum systems can undergo a measurement-induced phase transition (MIPT) in the entanglement properties of each individual quantum trajectory conditioned on the measurement outcomes [25–30]. For infrequent measurements $p < p_c^{\text{MIPT}}$, the unitary entangling dynamics dominate and the system remains volume-law entangled, whereas for sufficiently frequent measurements $p > p_c^{\text{MIPT}}$, local measurements collapse the many-body wavefunction and lead to area-law entangled states, a manifestation of quantum Zeno effect. Despite the exponentially costly post-selection of measurement outcomes, MIPT has been experimentally observed across multiple quantum platforms [31–33].

While measurement-induced entanglement transitions can only be observed upon unravelling the individual quantum trajectories by post-selecting a specific set of measurement outcomes, incorporating feedback operations further enriches the landscape of non-equilibrium phenomena in such hybrid systems [34–45]. More specifically, one adaptively controls the subsequent dynamics depending on each measurement outcome. A concrete example is quantum error-correction, where a corrective

* zhongyp@sustech.edu.cn

† chenaad@bc.edu

‡ zcyang19@pku.edu.cn

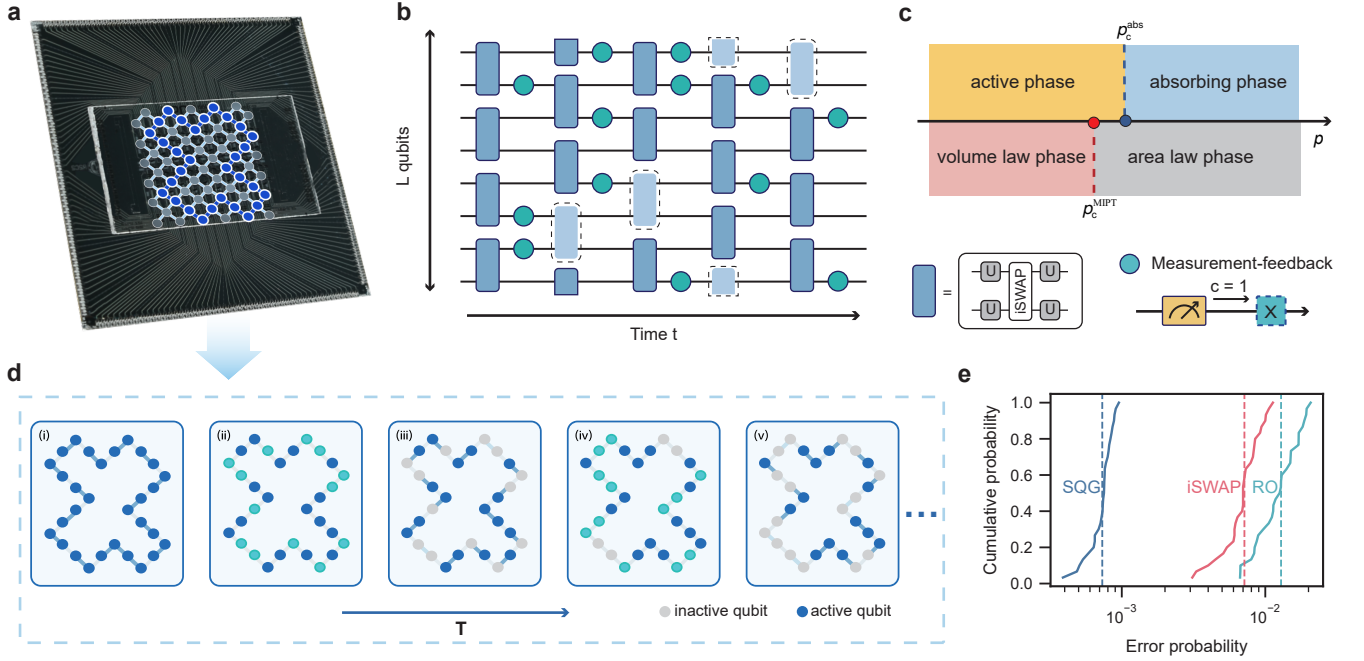


FIG. 1. **Quantum processor and adaptive quantum circuit for measurement-feedback dynamics.** **a**, The superconducting quantum processor used in this work. The device hosts 66 transmon qubits arranged in a 6×11 lattice, with 30 qubits (highlighted in blue) selected for the experiment to minimize crosstalk and enable high-fidelity mid-circuit operations. **b**, Schematics of the adaptive quantum circuit, consisting of alternating layers of two-qubit unitaries and mid-circuit measurements followed by real-time conditional feedback. The two-qubit unitaries are implemented using iSWAP-like entanglers dressed by random equatorial $\pi/2$ phase rotations (denoted by U). **c**, Phase diagram illustrating the measurement-and feedback-driven non-equilibrium phase transitions as the measurement rate p is varied. **d**, Illustration for the experimentally executed sequence of the adaptive circuit for the initial state where all sites are occupied. During the evolution, the classical flag variables dynamically track active and inactive qubits under the adaptive feedback protocol. Each labeled step (i, ii, iii, ...) consists of a unitary-evolution layer followed by a measurement-feedback layer. **e**, Cumulative error distributions for synchronized SQG, iSWAP, and mid-circuit RO operations, with median error rates of 0.07%, 0.7%, and 1.3%, respectively.

unitary is either applied or not depending on the error syndrome measurement outcomes. It has been shown in recent studies that a sufficiently large measurement and feedback rate $p > p_c^{\text{abs}}$ steers the system into a specific target state in a time that scales at most polynomially in system size (absorbing-phase), whereas for $p < p_c^{\text{abs}}$ the system remains ‘active’ (non-absorbing) for exponentially long time [35–39]. Notably, since the target state is an absorbing-state of the quantum channel, this transition can be observed at the level of averaged density matrix without postselection, and hence is distinct in nature from the entanglement transition. Indeed, it has been argued that under adaptive quantum dynamics, the entanglement transition and absorbing-state transition generically occur at different critical parameters, with the latter typically appearing at a higher measurement rate [35].

Despite the intensive theoretical investigations, experimentally realizing both the entanglement transition and absorbing-state transition in one quantum platform has remained challenging. This is because both transitions require a sufficiently large number of qubits to suppress finite-size effects, as well as high-fidelity gates and low-latency real-time measurement-feedback operations to

preserve coherent dynamics. Although a dissipation-driven non-equilibrium phase transition has been previously observed using a trapped-ion quantum simulator with mid-circuit measurements and qubit reuse [46], no active classical feedback operation was performed. In this work, we probe both transitions on a superconducting quantum processor, by leveraging the ability to perform high fidelity mid-circuit measurements and feedback within a sub-microsecond timescale (~ 700 ns for measurement and ~ 200 ns for the feedback branch) on our hardware. Using a system of 30 superconducting qubits augmented with classical ‘flag’ variables, we directly observe a transition between an absorbing phase where the total number of active qubits vanish after a very short circuit depth, and an active phase where the steady states host a finite density of active qubits. By choosing different initial states, we extract a set of critical exponents at the transition point which show excellent agreement with the directed percolation (DP) universality class. Moreover, using the same circuit architecture with 8 qubits, we further observe a measurement-induced entanglement transition from volume-law to area-law scaling. Crucially, we clearly find that the critical points of these

two transitions occur at well-separated tuning parameters with $p_c^{\text{MIPT}} < p_c^{\text{abs}}$, as expected on physical ground.

II. MODEL AND CIRCUIT ARCHITECTURE

A. Adaptive quantum circuit

Our quantum circuit consists of alternating layers of nearest-neighbor two-qubit unitary gates arranged in a brickwork pattern, followed by single-qubit Pauli- Z measurements on a one-dimensional chain of L qubits with periodic boundary conditions, as illustrated in Fig. 1b. The unitary layers alternate between odd and even bonds, such that each gate acts only on odd (or even) links within a given layer. For convenience, we interpret the local computational basis state $|1\rangle$ as an occupied site (one particle) and $|0\rangle$ as empty. We take the fully empty configuration $|\psi_t\rangle = |00\cdots 0\rangle$ as our target absorbing state. That is, the dynamics drives the system towards $|\psi_t\rangle$ but cannot leave it.

During each measurement step, if the outcome is $|0\rangle$, no action is taken; if the outcome is $|1\rangle$, a corrective Pauli- X gate is applied to that qubit. This feedback operation steers the system toward the target state $|\psi_t\rangle$, whereas the unitary gates can locally drive it away and do not preserve $|\psi_t\rangle$. To enable an absorbing-state phase transition, we introduce a classical flag variable f_i for each qubit (see Appendix B), taking values $f_i = 1$ (active) or $f_i = 0$ (inactive) [37, 38]. The flags are initialized according to the chosen initial state. After each measurement (and possible feedback), the measured qubit's flag is set to $f_i = 0$. A two-qubit unitary is applied on bond $(i, i+1)$ only if at least one of the two qubits is active, after which both flags are reset to $f_i = f_{i+1} = 1$. When both are inactive ($f_i = f_{i+1} = 0$), no unitary is applied, leaving the local subspace $|00\rangle$ invariant.

This hybrid quantum circuit, augmented by the flag variables, exhibits an absorbing-state transition in the quantum channel and a measurement-induced entanglement transition at the level of individual quantum trajectories (Fig. 1c). Alternative approaches to realizing such transitions have been proposed in Refs. [35, 36], where the unitaries are constrained to have a block structure that preserves a specific invariant subspace. In this work, we focus on the flag-based mechanism, as it is experimentally simpler to implement.

B. Implementation on a superconducting quantum processor

The experiment was performed on a 66-qubit superconducting quantum processor based on frequency-tunable transmon qubits arranged in a 6×11 lattice [47]. Nearest-neighbor interactions are mediated by tunable couplers, and all qubits are individually addressable through dedicated microwave and flux-control lines. From this de-

vice we select a 30-qubit subarray forming an X-shaped one-dimensional chain with periodic boundary conditions (Fig. 1a), which distributes active qubits across different readout groups to ensure high-fidelity simultaneous mid-circuit measurements. The device architecture and qubit-selection procedure are described in Appendix H.

The hybrid circuit dynamics consist of alternating nearest-neighbor entangling layers and probabilistic measurement-feedback layers (Fig. 1b,d). Each unitary layer is implemented using fSim-type entangling gates operated near the iSWAP point, dressed with local single-qubit rotations; in practice, discrete equatorial $\pi/2$ pulses are applied before and after each iSWAP-like entangler to control its residual phases and generate locally randomized unitary dynamics. After each unitary layer, active qubits are independently selected with probability p for a projective Z -basis measurement, and the digitized measurement outcomes are processed in real time by the field programmable gate array (FPGA)-based controller. When the outcome corresponds to the $|1\rangle$ state (classical bit $c = 1$ in Fig. 1b), a conditional X -reset pulse is applied to return the qubit to $|0\rangle$, completing the measurement-feedback cycle with sub-microsecond latency (~ 200 ns for real-time decision latency and ~ 50 ns for reset gate implementation). Representative performance metrics of the single-qubit gates (SQG), iSWAP gates, and mid-circuit readout (RO) are shown in Fig. 1e, with typical fidelities of $\sim 99.9\%$, 99.3% , and $\sim 98.7\%$, respectively. Further details on gate implementation and calibration are summarized in Appendix H, while details on measurement and feedback calibration are presented in Appendix G. These performance levels ensure that the hybrid circuit dynamics are faithfully implemented on the superconducting processor.

The absorbing-state transition can be captured by an order parameter corresponding to the average particle number in the system $N(t) = \sum_i n_i(t)$, where $n_i = 1$ for an occupied site and 0 for an empty site. Since the expectation value of $N(t)$ is linear in the density matrix, there is no need to post-select on the measurement outcome and one can simply compute $\langle N(t) \rangle$ by averaging over all measurement outcomes. For each measurement rate p and each circuit depth, we execute 100 independent random circuit instances. For each circuit realization, we sample 10,000 quantum trajectories. We then obtain $\langle N(t) \rangle$ as a function of circuit depth by averaging over both quantum trajectories and circuit realizations.

III. RESULTS

A. Absorbing-state transition

We start from the initial state with a single active site in the middle of the system $|\psi_0\rangle = |0\cdots 010\cdots 0\rangle$, and evolve under the hybrid quantum circuit with the protocol described above. At each step, two-qubit unitary gates are applied subject to constraints from the classi-

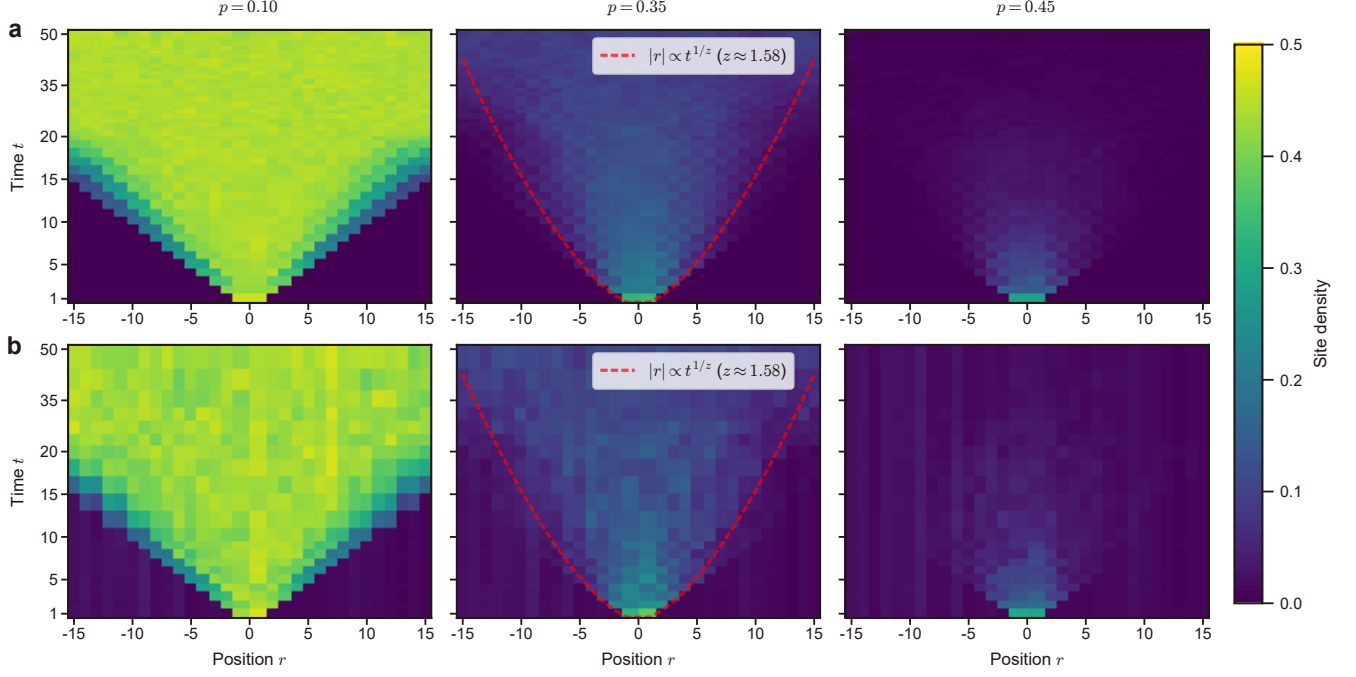


FIG. 2. **Absorbing-state transition in the adaptive quantum circuit.** **a, Numerical simulation.** Spatiotemporal profile of the local occupation $\langle n_i(t) \rangle$ for different measurement rates p via tDMRG simulations. We choose the initial state with a single occupied site in the middle $|\psi_0\rangle = |0 \dots 010 \dots 0\rangle$. Infrequent measurement ($p = 0.10$) yields a ballistically spreading active cluster, while sufficiently frequent measurement ($p = 0.45$) rapidly drives the system into the absorbing state with no particle. At the critical point ($p_c^{\text{abs}} \simeq 0.35$), the spreading becomes sub-ballistic with a lightcone satisfying $|r| \propto t^{1/z}$ with a dynamical exponent $z \approx 1.58$, consistent with DP universality class. **b, Experiment.** Measured spatiotemporal profile of $\langle n_i(t) \rangle$ on the 30-qubit processor shows excellent agreement with numerical simulations. Each figure was obtained by averaging over 100 random circuit instances and 10,000 trajectories for each circuit.

cal flags, followed by mid-circuit measurements and possible feedback operations. We evolve the system for a varying circuit depth up to $t_{\text{max}} = 50$ before reading out all qubits in Pauli-Z basis, which gives a spatiotemporal profile of the particle configurations upon averaging over trajectories and circuit realizations, as shown in Fig. 2 (lower panel). The experimental data clearly demonstrate two distinct phases at small and large measurement rates, respectively. When p is small ($p = 0.1$ in Fig. 2), the system is in an active phase where the initial seed spreads ballistically and forms a linear lightcone in spacetime. For the system size we experimentally probe, the total particle number saturates around $t \approx 20$, and this finite density of particles persists at later times up to $t_{\text{max}} = 50$. This is in stark contrast to the case of larger p ($p = 0.45$), where the total particle number increases only a little bit before quickly decaying to zero. This is the absorbing phase where the measurement and feedback operations succeed in steering the system towards the target state $|\psi_t\rangle$. At the critical point $p_c^{\text{abs}} \approx 0.35$, the particles spread sub-ballistically in time, showing a sub-linear lightcone structure. We find that the front of this spread follows the scaling $|r| \sim t^{1/z}$, where the fitted dynamical exponent $z \approx 1.58$. This exponent agrees with that in the DP universality class [48] (see Appendix

A for a summary of critical exponents at DP criticality). The experimental results are further corroborated by tDMRG simulations of the actual circuits executed on the quantum hardware (Fig. 2 upper panel).

In Fig. 3, we plot the average total particle number $N(t)$ in the two phases as well as at the transition point. For $p = 0.10$, the total number of active sites $N(t)$ initially increases and then saturates to a steady value, characteristic of the active phase. For $p = 0.45$, the particle number remains approximately constant for a short period before decaying towards zero, with a small residual density (~ 0.1) persisting due to experimental imperfections. Interestingly, at the critical point the total particle number exhibits an algebraic growth in time: $N(t) \sim t^\Theta$, with the fitted exponent $\Theta \approx 0.31$. The experimental data are consistent with numerical simulations of the same circuits executed experimentally. Remarkably, the exponent Θ is also in excellent agreement with that in DP [48], further suggesting that the transition we observed experimentally belongs to the DP universality class.

To further corroborate the nature of this absorbing-state transition, we perform a complementary set of experiments with a different choice of initial state where all sites are occupied $|\psi_0\rangle = |11 \dots 1\rangle$, from which we

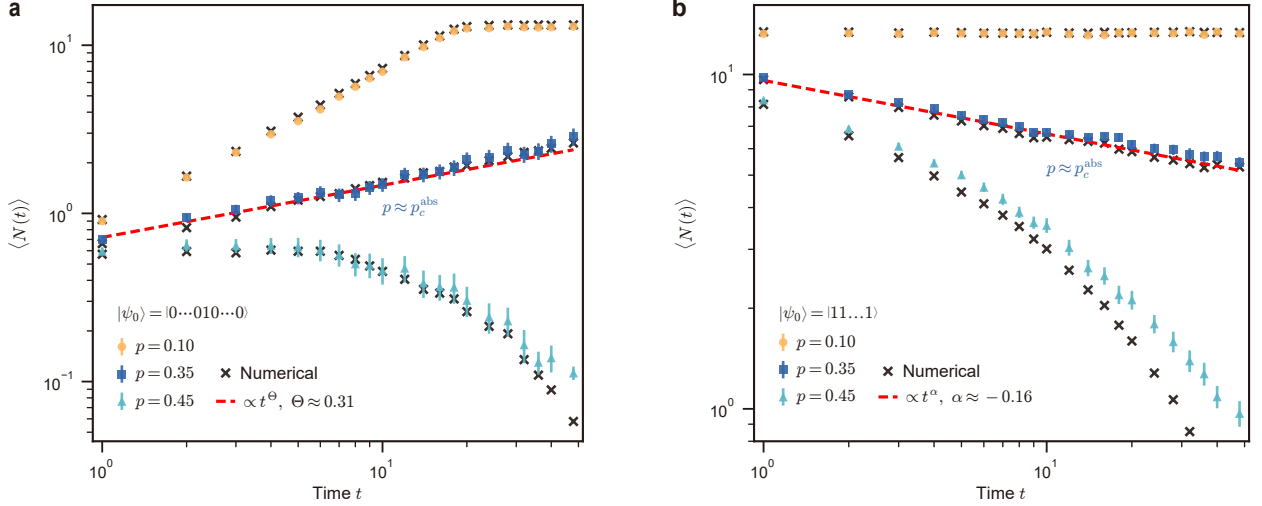


FIG. 3. **Critical exponents in directed percolation dynamics.** **a**, Time evolution of the average total particle number $N(t)$ for the initial state with a single occupied site in the middle $|\psi_0\rangle = |0\dots 010\dots 0\rangle$. **b**, Time evolution of $N(t)$ for the fully occupied initial state $|\psi_0\rangle = |11\dots 1\rangle$. In both panels, results are shown for three representative feedback rates: $p = 0.10$ (active phase), $p \approx 0.35$ (critical point), and $p = 0.45$ (absorbing phase). Colored symbols represent experimental data (averaged over 100 random circuit instances), and black crosses denote numerical simulations. Error bars indicate one standard error of the mean, obtained via bootstrap resampling, and are smaller than the symbol size when not visible. The fit for the critical exponents Θ , α is most reliable for $t < 20$, with deviations at later times due to finite-size effects.

also extract another critical exponent. As shown in Fig. 3b, in the active regime ($p = 0.10$) the particle density remains essentially constant throughout the evolution, characteristic of a sustained active phase. In the absorbing regime ($p = 0.45$), the number of active sites rapidly decays toward zero, with a small residual density persisting due to experimental imperfections. Near the critical point ($p_c^{\text{abs}} = 0.35$), the particle density decays algebraically in time as $n(t) \sim t^\alpha$, with an exponent $\alpha \approx -0.16$. This critical exponent also shows excellent agreement with predictions from one-dimensional DP universality class [48]. Taken together, our experimental observations, supported by numerical simulations, clearly demonstrate a measurement- and feedback-driven absorbing-state transition in our quantum device, belonging to the DP universality class.

B. Entanglement transition

To probe the measurement-induced entanglement transition on our hardware, we implement a reduced eight-qubit version of the hybrid circuit. The smaller system allows for full trajectory-level postselection while preserving the alternating unitary–measurement structure and the key dynamical features of the 30-qubit architecture. During the measurement windows, idle qubits are protected by a dynamical-decoupling sequence (DD), which suppresses dephasing accumulated while other qubits are being measured [49, 50]. For each trajectory, we perform quantum-state tomography to reconstruct reduced density matrices of subsystems of vari-

ous sizes, providing direct access to their entanglement properties (Fig. 4a). To achieve sufficient statistical resolution—particularly for estimating the variance of the entanglement entropy—we collect data from 150 random circuit instances.

Since the absorbing-state transition point identified above is around $p_c^{\text{abs}} \approx 0.35$, we scan a sufficiently broad interval of measurement rates $p \in [0, 0.4]$ to locate the position of the entanglement transition. For each p , the circuit depth and the number of randomized instances are chosen based on numerical simulations (see Appendix E). To quantify entanglement, we reconstruct the reduced density matrix of a contiguous three-qubit subsystem ($|A| = 3$) via quantum-state tomography on the final state, from which we compute the second Rényi entropy

$$S_A^{(2)} = -\log(\text{Tr } \rho_A^2),$$

where ρ_A is the reduced density matrix of subsystem A .

Fig. 4b shows the circuit and trajectory averaged second Rényi entropy $\langle S_A^{(2)} \rangle$ as a function of the measurement rate p . The result shows a monotonic decrease of entanglement with increasing p , consistent with our expectation. Since experimental noise introduces a spurious residual classical contribution that biases the raw entropy upward, we implement a two-step error-mitigation procedure. First, tomographic outcomes are corrected using the measured readout calibration matrix (readout inversion). Second, a residual baseline entropy was estimated by measuring the system in the limit $p = 1$ and subsequently subtracted from all data (residual-entropy mitigation). After the above two steps, the error-

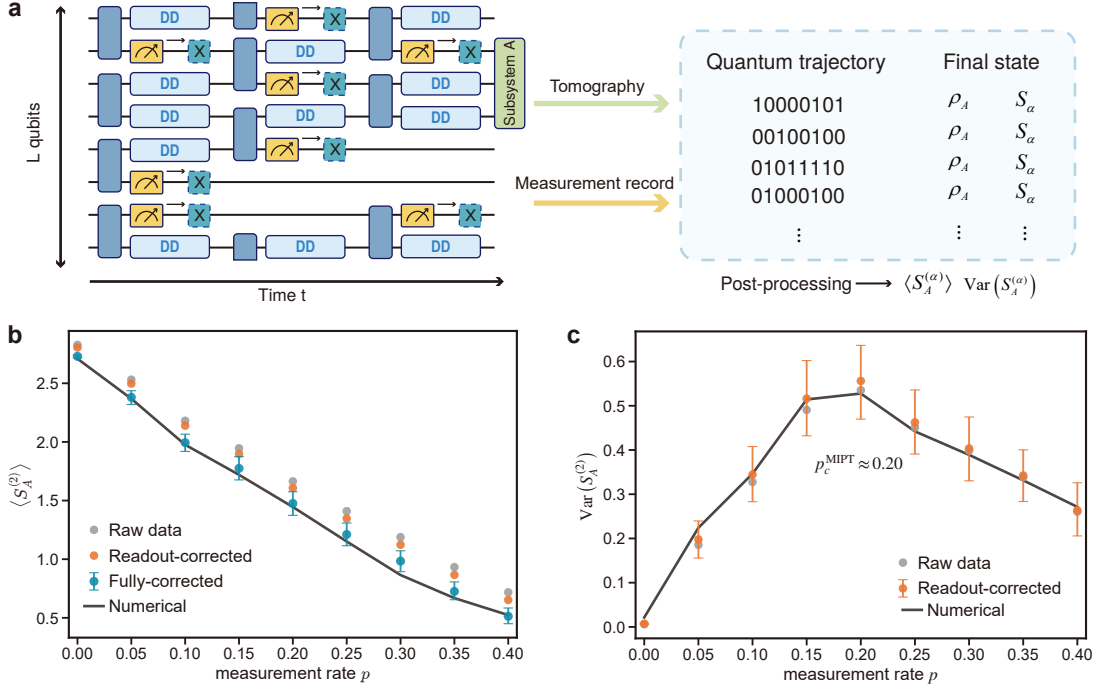


FIG. 4. **Measurement-induced entanglement transition.** **a**, Eight-qubit hybrid circuit used to probe the measurement-induced entanglement transition. It preserves the alternating unitary–measurement structure of the 30-qubit architecture, with idle qubits protected by dynamical decoupling during measurement windows. Mid-circuit measurement outcomes are recorded, and the reduced density matrix ρ_A on a three-qubit subsystem A conditioning on the measurement outcome is obtained via quantum state tomography. **b**, Average second Rényi entropy $\langle S_A^{(2)} \rangle$ versus measurement rate p . Experimental data (dots), corrected for readout errors and residual offsets, agree with numerical simulations (solid line) and show a monotonic suppression of entanglement with increasing p . **c**, Variance of $S_A^{(2)}$ $\text{Var}(S_A^{(2)})$ across random circuit instances. The variance exhibits a clear peak near $p \approx 0.20$, which we identify as the measurement-induced entanglement transition. Error bars represent 90% bootstrap confidence intervals.

mitigated experimental data are consistent with numerical simulations within the quoted uncertainties (see Appendix F for a detailed description of the error mitigation procedure).

To determine the location of the measurement-induced entanglement transition, we analyze the variance of the second Rényi entropy, $\text{Var}(S_A^{(2)}) = \langle (S_A^{(2)})^2 \rangle - \langle S_A^{(2)} \rangle^2$ across randomized circuit instances and quantum trajectories (Fig. 4c). Based on previous theoretical studies, the variance of $S_A^{(2)}$ develops a pronounced maximum near the critical point and thus provides a diagnostic for the transition [51]. After applying the same error-mitigation procedure, the measured variance shows a clear maximum near $p_c^{\text{MIPT}} \approx 0.20$, in agreement with numerical simulations within the experimental uncertainty. This peak signals the location of the entanglement transition. We have also analyzed Rényi entropies with different Rényi indices $\alpha = 1 - 4$, and the peaks of the variances of all Rényi entropies we consider yield a consistent estimate for the entanglement transition point around $p_c^{\text{MIPT}} \approx 0.20$ (Appendix D).

Importantly, the entanglement transition occurs at a substantially lower measurement rate ($p_c^{\text{MIPT}} \approx 0.20$) than the absorbing-state transition extracted from

particle-density measurements ($p_c^{\text{abs}} \approx 0.35$). This separation demonstrates that the loss of quantum correlations precedes the onset of the macroscopic absorbing-state transition in the feedback-driven circuit. Such a separation of these two transitions was previously suggested theoretically based on numerical simulations of hybrid Haar-random or Clifford circuit models [35–38] and hybrid free fermion systems [39], and to the best of our knowledge, our results provide its first direct experimental observation on a quantum device. Notice that the precise values of $(p_c^{\text{MIPT}}, p_c^{\text{abs}})$ depend on the particular gate set used, and are subject to uncertainties arising from the finite subsystem size, the overhead of tomography, and residual experimental noise. In Appendix C, we provide numerical evidence suggesting that the 30-qubit system also enters the area-law entangled phase well before $p_c^{\text{abs}} = 0.35$.

IV. DISCUSSION AND OUTLOOK

By integrating high-fidelity mid-circuit measurements and low-latency real-time conditional feedback, we realize a hybrid circuit architecture that supports both feedback-

driven absorbing-state transitions and measurement-induced entanglement transitions within the same superconducting quantum processor. Using up to 30 qubits, we directly observe the absorbing-state transition and extract critical exponents consistent with the DP universality class, while a smaller 8-qubit realization reveals a distinct entanglement transition at a lower measurement rate. The clear separation of these two critical points establishes that entanglement suppression and steering of quantum trajectories are fundamentally distinct phenomena in adaptive quantum circuits realized on noisy quantum hardware.

Beyond their conceptual significance, our results highlight the broader potential of measurement-feedback dynamics as a resource for controlling quantum information flow and exploring stochastic many-body phenomena in programmable quantum hardware. The same capabilities underpin emerging architectures for active quantum error correction and adaptive quantum algorithms, where feedback serves both as a stabilizing mechanism and as a control knob for engineering desired quantum states. Future experiments extending these ideas to higher-dimensional lattices, continuous monitoring, or feedback based on multi-qubit correlations may uncover new universality classes and dynamical regimes at the interface of quantum information and statistical mechanics.

ACKNOWLEDGEMENTS

This work is supported by Grant No. 12375027 from the National Natural Science Foundation of China (S.W. and Z.-C.Y.), the National Natural Science Foundation of China (12374474), the Innovation Program for Quantum Science and Technology (2021ZD0301703), the Science, Technology and Innovation Commission of Shenzhen Municipality (KQTD20210811090049034) and the Guangdong Basic and Applied Basic Research Foundation (2024A1515011714). Numerical simulations were performed on the High-performance Computing Platform of Peking University.

Author contributions

X.C. and Z.-C.Y. conceived and supervised the project. Z.W. calibrated the quantum processor and executed the experiment supervised by Y.Z. X.S. and J.Z. designed the electronics control system with fast feedback. S.W. and Z.W. performed numerical simulations of the circuits. Z.W., X.C. and Z.-C.Y. analyzed the experimental data and interpreted the results. Z.W., S.W., X.C., Z.-C.Y. and Y.Z. wrote the manuscript. All authors contributed to the discussion of the experiment and the preparation of the manuscript.

Competing interests

The authors declare no competing interests.

Data availability

The data that support the plots within this paper and other findings of this study are available from the corresponding authors upon reasonable request.

Appendix A: DP universality class

In our quantum circuit, the classical dynamics associated with the quantum channel can be mapped to a stochastic process in which particles (A) can diffuse, branch (create offspring), or annihilate [48]. The basic reactions are:

- Branching: $A \rightarrow 2A$ (rate: σ)
- Annihilation: $A \rightarrow \emptyset$

Depending on the reaction rates, the system exhibits a transition between an *active phase* (a steady state with a finite particle density) and an *absorbing phase* (where all particles eventually disappear). This transition belongs to the directed percolation (DP) universality class. The critical point occurs at a branching rate σ_c , which separates the active phase ($\sigma > \sigma_c$) from the absorbing phase ($\sigma < \sigma_c$). At the critical point ($\sigma = \sigma_c$), the system displays scale-invariant dynamics whose properties depend on the initial conditions. Below, we examine two types of initial conditions for a one-dimensional system at criticality.

Two commonly used initial conditions are considered when studying critical dynamics:

1. **Single-Seed Initial Condition:** Starting from a single active site, it can grow into an active cluster in the spatial and temporal direction. The average number of particles grows as a power law in time (at early time):

$$\langle N(t) \rangle \sim t^\Theta, \quad \Theta \approx 0.3138.$$

The spatial extent of the active cluster is characterized by the mean-square spreading,

$$\langle R^2(t) \rangle \sim t^{2/z},$$

where $z \approx 1.581$ is the dynamical exponent relating space and time via $t \sim L^z$.

2. **Fully Active Initial Condition:** When all sites are initially active (or occupied with a nonzero probability $\rho_0 < 1$), the particle density decays as

$$\langle \rho(t) \rangle \sim t^{-\alpha}, \quad \alpha \approx 0.1595.$$

Appendix B: Classical flag

The original theoretical proposal of adaptive quantum circuits involves local unitary gates with a block structure, leaving a particular subspace that is locally similar to the target state invariant [35, 36]. Implementation of such unitaries would require a decomposition (compilation) in terms of a set of elementary single-and-two-qubit unitaries that are conveniently executed experimentally. This introduces a huge overhead in terms of the number

of gates and circuit depth. To circumvent this problem, we introduce a classical flag variable f_i associated with each qubit that takes value 0 (labeling an ‘inactive’ qubit) or 1 (labeling an ‘active’ qubit), following the method introduced in Ref.[37, 38]. A subsequent entangling gate can only be applied if at least one of the two qubits is active. For the fully active initial state $|\psi_0\rangle = |11\dots 1\rangle$, we set $f_i = 1$ for all i initially. For the single-seed initial state $|\psi_0\rangle = |0\dots 010\dots 0\rangle$, we set $f_i = 1$ only for the occupied site and $f_i = 0$ for all other sites initially.

For each unitary layer, we apply an entangling gate if at least one of (f_i, f_{i+1}) is 1. We then reset $f_i = f_{i+1} = 1$ after the gate is applied. For each measurement layer, we set $f_i = 0$ for the measured qubit. One can easily see that the dynamics of the flag variables themselves satisfy the stochastic classical process described above, and hence exhibit a classical non-equilibrium phase transition in DP universality class. We have also verified this directly in our experiment (data not shown). On the other hand, for the quantum system, since we know that qubits labelled as inactive must be in $|0\rangle$ state whereas those labelled as active typically have a non-zero probability of being in $|1\rangle$ state, we expect that the actual order parameter of the quantum system also inherits the same DP phase transition. Indeed, our results confirm that the quantum order parameter and the classical flag variable exhibit the same DP phase transition under the adaptive dynamics.

Appendix C: tDMRG simulation method

We numerically simulate the random adaptive quantum circuits described in Sec. II A using the time-evolving density matrix renormalization group (tDMRG) method. Each quantum trajectory is represented as a matrix product state (MPS), with the bond dimension chosen to ensure numerical convergence. Projective measurements are implemented by first computing the Born probabilities from the occupation numbers of the designated measured qubits and then randomly selecting the subsequent trajectory according to these probabilities. After determining the measurement outcome, we apply the corresponding feedback operation: if the outcome is “empty,” the MPS is projected onto the empty state; if it is “occupied,” the MPS is projected onto the occupied state and then subjected to a Pauli- X rotation to reset the qubit to the empty state. After each time step, the MPS is truncated to a maximum bond dimension of $\chi = 64$ and renormalized to compensate for the norm loss introduced by projection. For each circuit instance, we average observables over 50 independent trajectories, and the final results are obtained by averaging these trajectory-averaged quantities over all 500 realizations of the adaptive circuit ensemble.

In our experiment, the entanglement transition was probed using a smaller system size of eight qubits due to the significant overhead from postselection. Here we provide numerical evidence suggesting that the orig-

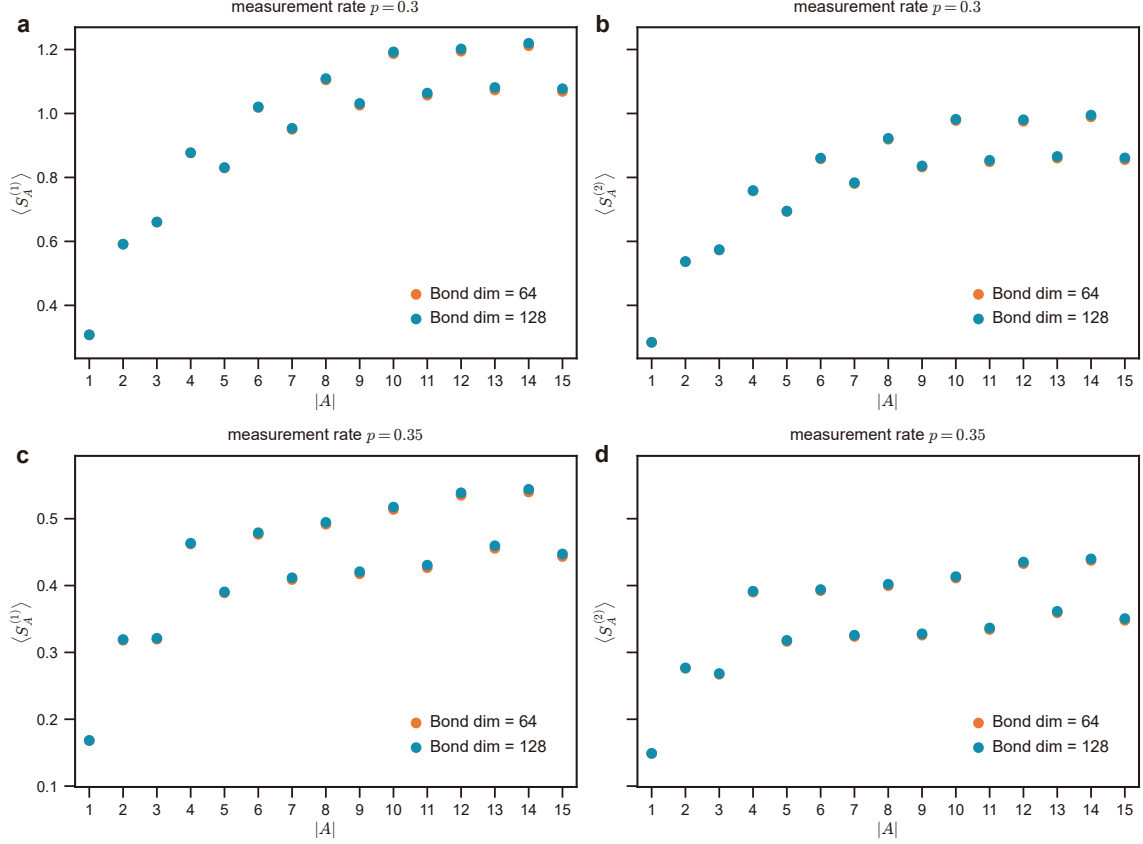


FIG. 5. **Scaling of entanglement entropy of the steady states.** Numerical tDMRG simulation of the averaged von-Neumann entanglement entropy $\langle S_A^{(1)} \rangle$ (a,c) and the second Rényi entropy $\langle S_A^{(2)} \rangle$ (b,d) as a function of subsystem size $|A|$, for the same 30-qubit quantum circuits used experimentally for probing absorbing-state transition. **a,b**, measurement rate $p = 0.3$. **c,d**, measurement rate $p = 0.35$. The entanglement entropy exhibits area-law scaling already at $p = 0.30 < p_c^{\text{abs}}$. The results for different choices of bond dimension $\chi = 64$ and $\chi = 128$ are almost identical, confirming numerical convergence.

inal 30-qubit system also enters the area-law entangled phase well before the absorbing-state transition at $p_c^{\text{abs}} = 0.35$. By constructing the reduced density matrix from the MPS, we numerically evaluate the bipartite von-Neumann entropy and the second Rényi entropy for the steady states of a system of 30 qubits and subsystem sizes $|A|$ ranging from 1 to 15, as shown in Fig. 5. The results are averaged over 10 independent trajectories for each of the 500 circuit realizations. We find that indeed the subsystem entanglement saturates for large $|A|$ already at $p = 0.30$, showing an area-law scaling. Furthermore, the numerical results for bond dimension $\chi = 64$ and $\chi = 128$ are almost identical, indicating that a choice of $\chi = 64$ is sufficient to ensure convergence for our simulations.

Appendix D: Additional experimental data

1. Fully occupied initial state

Figure 6 shows the absorbing-state dynamics for the fully occupied initial state under the same measurement-

and-feedback circuit architecture used in the main text. This provides a complementary setup to the one shown in Fig. 2 of the main text starting from a single active site initially.

At low measurement rate ($p = 0.10$), the system remains active, exhibiting nearly uniform occupation throughout the evolution. At a near-critical measurement rate ($p = 0.35$), the site density shows a slow, algebraic temporal decay. For high measurement rate ($p = 0.45$), the population vanishes rapidly within only a few layers, consistent with the absorbing regime in which repeated measurements and feedback operations drive the system toward the target state exponentially fast. Residual late-time signals arise primarily from read-out misclassification and occasional leakage events during mid-circuit measurements. Together with the single active site initial condition in Fig. 2 of the main text, these results establish a consistent picture of an absorbing-state transition in our adaptive circuits.

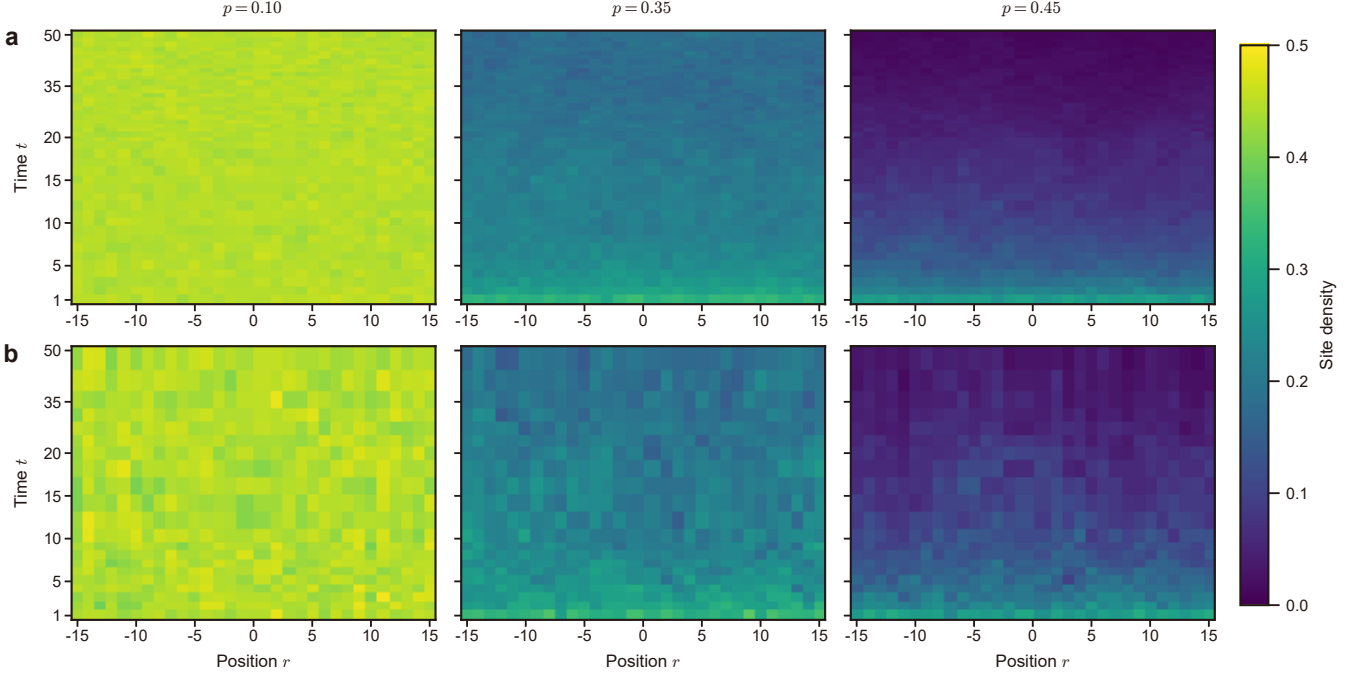


FIG. 6. **Absorbing-state transition from fully occupied initial state ($|1\rangle^{\otimes N}$).** **a, Numerical simulation.** Spatiotemporal profile of the local occupation $\langle n_i(t) \rangle$ for different measurement rates p via tDMRG simulations: $p = 0.10$ (active phase), $p = 0.35$ (near the critical point), and $p = 0.45$ (absorbing phase), with all qubits initialized in $|1\rangle$. In contrast to the single-site initialization in Fig. 2, the dynamics do not exhibit spatial spreading; instead, the occupation decays approximately uniformly in space, reflecting global relaxation induced by repeated measurements and feedback operations. **b, Experiment.** Measured spatiotemporal profile of $\langle n_i(t) \rangle$ on the 30-qubit processor under the same protocol. Each pixel represents the average occupation obtained from 100 randomized circuit instances and repeated measurement shots. Color encodes the normalized site density using the same scale as in Fig. 2 of the main text.

2. Entanglement transition for other Rényi entropies

In the main text we characterized the measurement-induced entanglement transition using the second Rényi entropy $S_A^{(2)}$ of a three-qubit subsystem A (Fig. 4b,c). Since the full reduced density matrices ρ_A are reconstructed via quantum-state tomography, the same data set also allows us to evaluate Rényi entropies of other orders $\alpha = 1, 3, 4$ without additional measurements,

$$S_A^{(\alpha)} = \begin{cases} -\text{Tr}(\rho_A \log \rho_A), & \alpha = 1, \\ \frac{1}{1-\alpha} \log(\text{Tr} \rho_A^\alpha), & \alpha \neq 1, \end{cases} \quad (\text{D1})$$

and we apply the same analysis and error-mitigation procedures as for $S_A^{(2)}$.

For all tested orders $\alpha = 1-4$, the average entropy $\langle S_A^{(\alpha)} \rangle$ decreases monotonically with the measurement rate p , while the variance $\text{Var}(S_A^{(\alpha)})$ exhibits a clear maximum near the same critical point $p_c^{\text{MPT}} \approx 0.20$. Although all orders display the same global trend, their detailed behaviors show a clear dependence on the Rényi order.

In particular, the first-order (von Neumann) entropy $S_A^{(1)}$ exhibits a noticeably larger deviation from ideal numerics even after full error mitigation. This behavior is expected because $S_A^{(1)}$ depends logarithmically on the complete eigenvalue spectrum of ρ_A and is therefore especially sensitive to reconstruction errors in the small-eigenvalue sector. Similar deviations at $\alpha = 1$ —despite correct qualitative scaling—have also been reported in previous mid-circuit measurement experiments [32].

In contrast, the higher-order Rényi entropies $S_A^{(3)}$ and $S_A^{(4)}$ are less sensitive to contributions from small eigenvalues and therefore show much better quantitative agreement with numerics after mitigation, yielding the same transition location as $S_A^{(2)}$ within experimental uncertainty. We further note that the peak position of $\text{Var}(S_A^{(\alpha)})$ displays mild α -dependent shifts. Nevertheless, the peak locations remain well separated from the absorbing-state transition at $p_c^{\text{abs}} \approx 0.35$, confirming that the two transitions are clearly distinct for all Rényi orders.

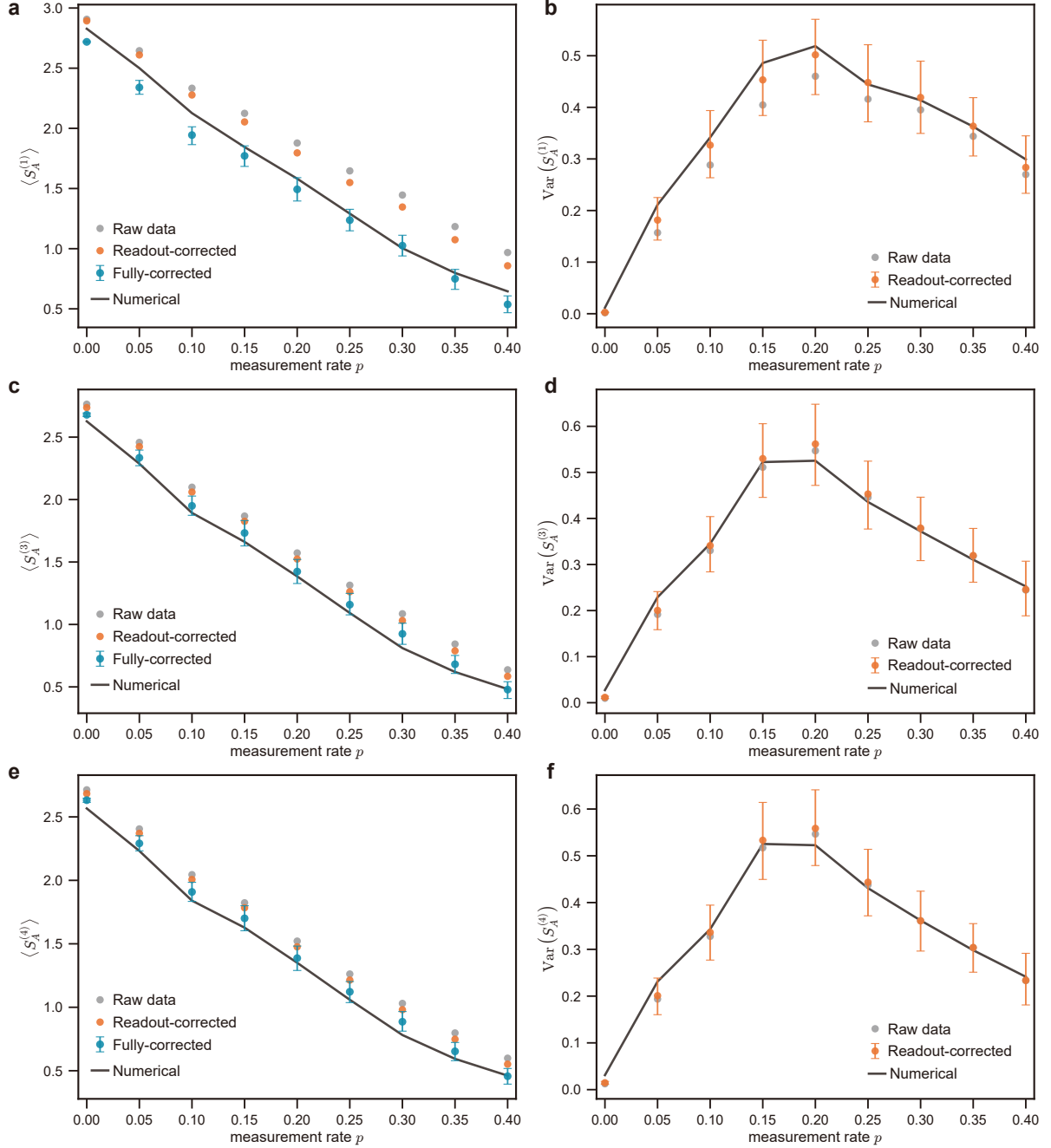


FIG. 7. **Entanglement transition at different Rényi orders.** **a,c,e**, Average entanglement entropy $\langle S_A^{(\alpha)} \rangle$ for $\alpha = 1, 3, 4$ as a function of measurement rate p . **b,d,f**, Variance of $S_A^{(\alpha)}$ $\text{Var}(S_A^{(\alpha)})$ for the same orders. All Rényi orders exhibit a monotonic decrease with p and a variance peak near a consistent entanglement transition point, while quantitative order-dependent differences are discussed in the text.

Appendix E: Additional experimental details on entanglement transition

1. Simulation setup and parameter selection

To capture the measurement-induced entanglement transition, we simulate the same hybrid-circuit model

used in the experiment and choose circuit parameters that make the transition clearly visible while keeping the sampling cost manageable. An important choice is the circuit depth: it must be large enough for the subsystem entanglement to reach a quasi-steady value, but not so deep that additional layers only add experimental overhead without altering the relevant behavior.

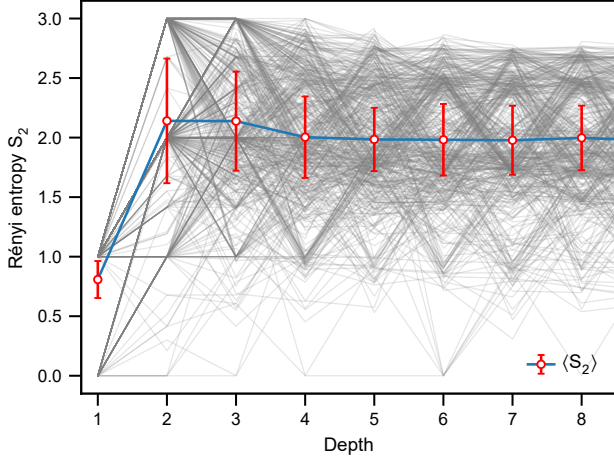


FIG. 8. **The second Rényi entropy versus circuit depth.** Depth dependence of the subsystem Rényi entropy $S_A^{(2)}$ at $p = 0.1$, obtained from 500 randomized circuit realizations. Each gray line corresponds to a different random circuit, while the blue line denotes the ensemble average, which quickly settles into a depth-independent value. The entropy becomes effectively saturated at a depth of about 4, illustrating the onset of the quasi-steady regime used to select the working depths in the main analysis.

To determine an appropriate circuit depth, we examine how the Rényi entropy evolves with depth across different measurement rates. As a representative illustration, Fig. 8 shows the depth dependence of the subsystem entanglement entropy $S_A^{(2)}$ at $p = 0.1$, evaluated from 500 randomized circuit realizations. Each gray line corresponds to a different random circuit, displaying considerable variation at small depth, while the ensemble-averaged entropy (blue line) rapidly settles into a steady trend. For this and other values of p , the entropy becomes essentially depth-independent once the circuit reaches a depth of about 4, indicating that subsystem entanglement has reached a quasi-steady regime, and that additional layers do not alter the behavior qualitatively. We therefore use depths in the range 1–4 for both simulation and experiment to access this regime without incurring unnecessary sampling overhead.

2. Details on tomography

Quantum state tomography (QST) [52] is used to reconstruct the reduced density matrix ρ_A of a small subsystem A from an informationally complete set of local measurements. For a k -qubit block, measuring the three Pauli axes on each qubit yields 3^k product bases that uniquely determine ρ_A up to statistical fluctuations. Once ρ_A is obtained, the Rényi entropies $S_A^{(\alpha)}$ for various orders α are directly evaluated from its eigenvalues.

In our experiment we target contiguous three-qubit

subsystems ($|A| = 3$). For each randomized circuit instance at a fixed measurement rate p , we measure all $3^3 = 27$ Pauli-product bases and aggregate over shots and instances to reconstruct ρ_A . This scheme provides full tomographic information while remaining experimentally tractable, enabling the extraction of $S_A^{(\alpha)}$ and the corresponding fluctuations across different Rényi orders.

3. Sampling strategy and runtime accounting

To improve data-acquisition efficiency, we first optimize the circuit execution schedule. In a conventional setup, each experimental cycle is followed by a long idle interval—typically several multiples of T_1 , corresponding to an effective reset time of $\sim 400 \mu\text{s}$ —to allow qubits to relax to the ground state $|0\rangle$. Here we shorten the inter-shot interval by combining an *active reset*—implemented using the same measurement–feedback operation described in the main text, applied once before each circuit to deterministically prepare $|0\rangle$ —with a short *passive reset* stage, during which the qubit–coupler configuration is biased to enhance energy dissipation through the readout resonator [53]. This hybrid reset protocol increases the experimental duty cycle while leaving the in-circuit hybrid dynamics unaffected, reducing the effective cycle time of each circuit to approximately $50 \mu\text{s}$.

With the reset optimization in place, we can sustain the large number of repeated measurements required for QST. For each value of p , we generate about 150 random circuit instances. Since extracting $S_A^{(\alpha)}$ requires full QST of a three-qubit subsystem, each circuit is measured in all $3^3 = 27$ Pauli-product bases. The number of shots per basis is chosen to ensure reliable reconstruction of ρ_A : in practice, for most quantum trajectories each tomographic basis is sampled more than 100 times.

The corresponding circuit depths, median and maximum numbers of mid-circuit measurements, total shots, and overall runtimes for each value of p are summarized in Table I. The full data-acquisition campaign spans approximately 200 hours and covers about 1500 randomized circuit instances across all p , providing sufficient statistics to extract the monotonic suppression of $S_A^{(\alpha)}$ with increasing p and to resolve the variance peak near $p_c^{\text{MIPT}} \approx 0.20$, while maintaining stable device performance throughout the experiment.

Appendix F: Error mitigation

1. Readout error mitigation.

In our superconducting platform, raw measurement outcomes exhibit state-dependent detection errors and residual crosstalk between qubits sharing the same readout feedline. To characterize these effects, we calibrate an assignment matrix on the tomographic subsystem by

p	Depth	Measurements Median (Max)	Shots (Approx.)	Random Circuits	Wall Time(h)
0.00	4	0(0)	1×10^4		
0.05	4	2(5)	2×10^4		
0.10	4	3(7)	5×10^4		
0.15	3	3(8)	5×10^4		
0.20	3	5(9)	5×10^4	$\approx 150 \times 10$	≈ 200
0.25	3	6(10)	1×10^5	$= 1500 \text{ total}$	
0.30	3	7(11)	1×10^5		
0.35	3	8(12)	1×10^5		
0.40	3	8(12)	1×10^5		
1.00	1	8(8)	1×10^5		

TABLE I. Experimental parameters and run statistics for the entanglement entropy measurements on hardware. For each measurement rate p , we list the circuit depth, the median (maximum) number of mid-circuit measurements per circuit, the approximate total number of measurement shots, and the number of randomized circuit instances. The rightmost columns indicate that the full data set comprises about 1500 random circuits and a total wall time of roughly 200 hours across all values of p .

preparing the relevant computational-basis states and measuring them through the same multiplexed readout chain used in the main experiment. This matrix captures the classical stochastic map between the prepared and measured outcomes [54, 55], including the dominant correlated errors within the subsystem.

In post-processing, we apply a regularized inverse (based on truncated-SVD) to this matrix to obtain corrected estimates of the outcome probabilities prior to state reconstruction. This procedure performs a classical deconvolution of the measurement noise and does not impose any assumptions about the underlying quantum dynamics. All “readout-corrected” data reported in Fig. 4 and Fig. 7 use this correction, while the “fully corrected” results additionally incorporate the residual-entropy procedure described in the next subsection.

2. Residual entropy correction

After applying readout-error mitigation, the entanglement entropies $S_\alpha(p)$ are extracted from readout-corrected tomographic data that already account for calibrated state-dependent detection errors and readout crosstalk. However, residual discrepancies remain due to incoherent processes such as energy relaxation and dephasing occurring during circuit execution, which introduce additional noise-induced mixedness into the reconstructed density matrices. These effects manifest as an additive positive offset in the entropy that does not originate from genuine many-body entanglement.

To correct for this effect, we follow the linear residual-entropy correction protocol introduced in Ref. [33]. The key idea is to use the measurement-only configuration ($p = 1$) as a reference, where the system should ideally

collapse into a fully disentangled product state with zero intrinsic entropy. Assuming that the magnitude of this residual contribution scales linearly with an effective total error budget of the circuit, the corrected entropy is expressed as

$$S_\alpha^{\text{corr}}(p) = S_\alpha(p) - \frac{\langle \mathcal{E}[\mathcal{C}_p] \rangle}{\langle \mathcal{E}[\mathcal{C}_{p=1}] \rangle} S_\alpha(p=1), \quad (\text{F1})$$

where $\langle \mathcal{E}[\mathcal{C}_p] \rangle$ denotes the average effective error budget of circuits at measurement rate p evaluated over random circuit instances, and $S_\alpha(p=1)$ is the corresponding entropy extracted from the readout-corrected data at $p = 1$. The effective circuit error $\mathcal{E}[\mathcal{C}_p]$ is estimated from the calibrated single-qubit, two-qubit, and readout error rates ($\epsilon_{1q}, \epsilon_{2q}, \epsilon_{ro}$), weighted by the average number of such operations appearing in the circuit at a given measurement rate p . In our experiment, the calibrated error rates are $\epsilon_{1q} \approx 7 \times 10^{-4}$, $\epsilon_{2q} \approx 7 \times 10^{-3}$, and $\epsilon_{ro} \approx 1.4 \times 10^{-2}$, which are used as the input parameters for this error-budget estimation. It can be approximately expressed as

$$\mathcal{E}[\mathcal{C}_p] \approx \epsilon_{1q} N_{1q}(p) + \epsilon_{2q} N_{2q}(p) + \epsilon_{ro} N_{ro}(p),$$

where $N_{1q}(p)$, $N_{2q}(p)$, and $N_{ro}(p)$ denote the mean counts of one-qubit gates, two-qubit gates, and measurement operations, respectively, in a single realization of the circuit at measurement rate p . The averaging $\langle \cdot \rangle$ over different random circuit instances is then performed to obtain $\langle \mathcal{E}[\mathcal{C}_p] \rangle$, which captures the overall error level corresponding to each experimental configuration. The reference value $S_\alpha(p=1)$ is directly measured on the same device and qubit subset to ensure a consistent calibration of this residual floor.

This linear correction removes the noise-induced en-

trophy offset arising from incoherent processes and yields a more accurate estimate of the mean entanglement entropy across different measurement rates p . While it slightly shifts the absolute values of $\langle S_\alpha \rangle$, it does not affect the entropy fluctuations or the extracted variance $\text{Var}(S_\alpha)$, from which the critical measurement point of the entanglement transition is determined. The fully corrected mean entropies are used in the entropy panels of Fig. 4b and in the multi-order entropy results of Fig. 7a,c,e, where an accurate absolute entropy scale is required for comparison with numerical simulations.

Appendix G: Feedback calibration and verification

1. Real-time feedback architecture

Our experiment employs adaptive quantum circuits in which mid-circuit measurements are followed by real-time classical processing and conditional quantum operations. Each feedback cycle consists of four sequential stages: (i) measurement acquisition, (ii) digitization and demodulation, (iii) real-time classification, and (iv) conditional actuation.

During the measurement acquisition stage, a readout pulse of approximately 500 ns is applied to the qubit's dispersively coupled resonator. To reliably extract the measurement outcome, we allocate an additional 200 ns in the demodulation window of the ADC-FPGA chain, accommodating the residual photon leakage of the readout resonator 150 ns and the 50 ns propagation time of the signal through the cables to the digitizer. Once the digitized record is available, the FPGA performs real-time processing of the measurement outcome. In our hardware the minimal achievable feedback latency is about 180 ns [56], but we employ a conservative fixed delay of 200 ns to synchronize the feedback timing across all 30 qubits. Finally, the conditional reset operation is delivered as a short 50 ns feedback pulse, completing the timing-aligned feedback branch across all qubits.

In total, these stages yield an end-to-end latency of approximately 950 ns for a full measurement-feedback cycle, which is far shorter than the qubit energy-relaxation time ($T_1 \sim 70\text{--}80\ \mu\text{s}$) and therefore compatible with coherent mid-circuit control. A detailed timing budget for both the measurement-only and feedback-enabled branches is summarized in Table II.

2. Mid-circuit measurement and feedback fidelity

We first characterize the fidelity of mid-circuit measurements, which serves as the baseline for evaluating the performance of feedback operations. As illustrated in Fig. 9, the calibration is based on a quantum-nondemolition (QND) protocol that permits repeated measurements of the same qubit without disturbing its state. Depending on whether the two measurements are

TABLE II. Timing budget of the real-time measurement and feedback cycle.

Process	Duration (ns)
Readout pulse (DAC)	500
Residual demodulation tail	200
FPGA synchronization delay	200
Conditional reset pulse	50
Total (measurement only)	700
Total (measurement + feedback)	950

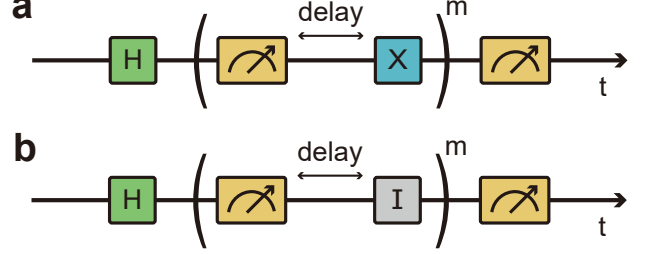


FIG. 9. Circuit used to calibrate the QND mid-circuit measurement fidelity. **a**, The X gate implements the π -QND configuration used for the $|1\rangle$ -state readout. **b**, Replacing this rotation with an identity operation yields the I-QND configuration for the $|0\rangle$ -state readout.

performed consecutively (“I-QND”) or with an intervening X gate (“ π -QND”), the protocol characterizes the readout fidelities of the $|0\rangle$ and $|1\rangle$ states, while suppressing the influence of residual thermal excitation and imperfect state preparation.

For the $|0\rangle$ state, we initialize the qubit in $|0\rangle$, perform a QND measurement, and postselect on $m_1 = 0$. We then define the ground-state QND fidelity as $F_0^{\text{QND}} = P(m_2 = 0 | m_1 = 0)$, where m_1 and m_2 denote the outcomes of the first and second measurements, respectively.

For the $|1\rangle$ state, we employ the π -QND protocol: after postselecting on $m_1 = 0$ from the first measurement, we apply a high-fidelity X gate to prepare $|1\rangle$ and perform a second QND measurement. The excited-state QND fidelity is defined as $F_1^{\text{QND}} = P(m_2 = 1 | m_1 = 0, X)$ and is mainly limited by energy relaxation during the readout interval. The overall mid-circuit measurement fidelity is then

$$F_{\text{meas}} = \frac{F_0^{\text{QND}} + F_1^{\text{QND}}}{2}. \quad (\text{G1})$$

Experimentally, $F_0^{\text{QND}} \approx 99.5\%$ and $F_1^{\text{QND}} \approx 98\%$, yielding an average mid-circuit measurement fidelity of about 98.7%. This corresponds to a median readout error of $\sim 1.3\%$, as summarized in Fig. 10.

Building upon the QND calibration, we characterize the fidelity of the feedback operation. The feedback protocol differs from QND readout only by the presence

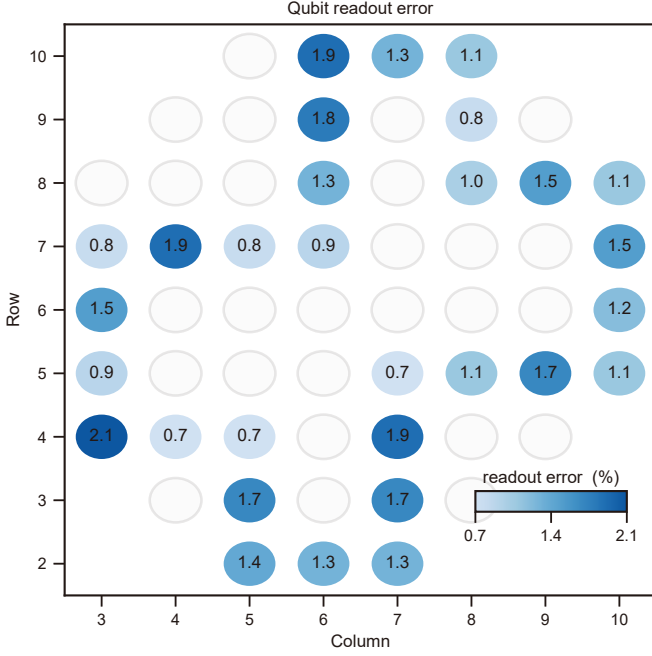


FIG. 10. **Readout error.** The values are obtained from simultaneous QND mid-circuit measurements performed across all 30 qubits used in the experiment.

of a fixed latency before the subsequent gate execution. To emulate the real hardware timing, we insert a programmable delay of approximately 200 ns between the mid-circuit measurement and the following operation. The ground-state branch is identical to I-QND and we set $F_0^{\text{fb}} = F_0^{\text{QND}}$. For the $|1\rangle$ branch, we use a delayed π -QND sequence: prepare $|1\rangle$, perform a QND measurement and postselect on $m_1 = 1$, wait for a delay τ_{fb} , apply an X gate to reset the state to $|0\rangle$, and perform a second measurement. The corresponding fidelity is defined as $F_1^{\text{fb}} = P(m_2 = 0 \mid m_1 = 1, \tau_{\text{fb}}, X)$, and the overall feedback fidelity is

$$F_{\text{fb}} = \frac{F_0^{\text{fb}} + F_1^{\text{fb}}}{2}.$$

Experimentally, the ground-state branch remains unchanged, while the $|1\rangle$ -branch feedback fidelity is about 97.3%, consistent with the expected relaxation over the calibrated delay. This yields an overall feedback-operation fidelity of approximately 98.4%.

Appendix H: Superconducting quantum processor and calibration

1. Experimental platform and qubit selection

The experiments are performed on a 66-qubit superconducting quantum processor operated in a dilution

refrigerator at millikelvin temperatures. The cryogenic setup, wiring configuration, and room-temperature control electronics follow the same design as reported in Ref. [57].

In this processor, the qubits form a 6×11 rectangular lattice of frequency-tunable transmons with nearest-neighbor coupling mediated by tunable couplers [47]. Along each vertical column, six qubits share a common readout resonator coupled to a single feedline, enabling frequency-multiplexed dispersive readout. Simultaneous readout within the same group can introduce correlated errors due to spectral crowding, amplifier nonlinearity, and residual crosstalk between qubits on the same feedline [58].

For the measurement–feedback experiments, we select 30 qubits from the full device. The selection aims to reduce the loading on each readout line and to minimize readout crosstalk by distributing the active qubits across different readout groups and placing qubits sharing the same resonator as far apart as possible on the lattice. This layout supports high-fidelity simultaneous mid-circuit measurements while maintaining the required connectivity for the experimental protocol.

2. Qubit parameters and frequency allocation

The frequency allocation of the 30 working qubits is primarily constrained by the presence of two-level-system (TLS) defects, which introduce coherence dips and unstable frequency regions. To ensure reliable operation, idle frequencies are chosen to avoid TLS hotspots and other unstable intervals identified from spectroscopy and time-domain measurements. In addition, each qubit must remain sufficiently detuned from its neighbors to prevent frequency collisions during flux tuning. Because the entangling operations require pairs of qubits to be tuned toward a common interaction frequency, qubits forming two-qubit gates are assigned idle frequencies that are reasonably close. Finally, qubits sharing a common readout resonator must be well separated in frequency at their idle points to suppress measurement-induced crosstalk during simultaneous mid-circuit readout.

The resulting frequency arrangement and coherence parameters are summarized in Fig. 11. Panel (a) shows the assigned idle qubit frequencies, typically around 4.2–4.4 GHz. Panel (b) displays the corresponding readout-resonator frequencies near 6.2 GHz. Panels (c) and (d) present the measured energy-relaxation times T_1 and Hahn-echo coherence times T_2^{echo} , which characterize the coherence performance of the selected qubits. These measurements define the stable frequency manifold used for simultaneous mid-circuit measurements and high-fidelity quantum-gate operations.

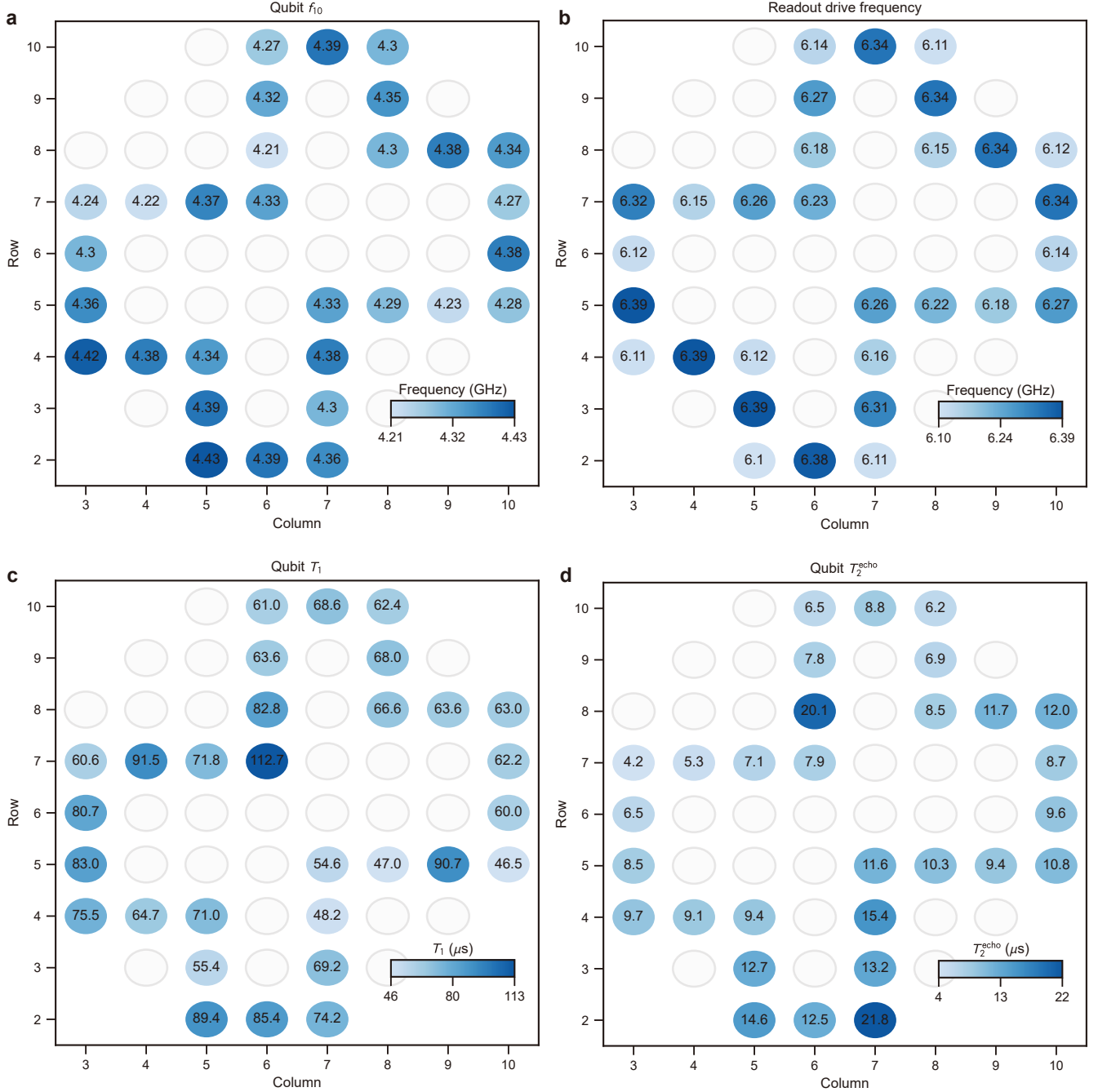


FIG. 11. **Qubit parameter map for the 30 qubits used in the experiment.** Data are taken from a 66-qubit superconducting processor arranged in a 6×11 lattice. For visualization, the lattice is shown in a 45° rotated orientation, where groups of six diagonally aligned qubits share a common readout line. **a**, Operating qubit frequencies f_q obtained from spectroscopy. **b**, Calibrated readout-drive frequencies of the corresponding resonators. **c**, Energy-relaxation times T_1 measured via exponential decay. **d**, Hahn-echo coherence times T_2^{echo} characterizing dephasing under echo refocusing.

3. Gate implementation and calibration

Single-qubit gates are implemented using Gaussian-DRAG microwave pulses [59, 60], with a nominal duration of 50 ns for a π rotation and 25 ns for a $\pi/2$ rotation

obtained by halving the pulse area. Two-qubit entangling operations are realized using tunable-coupler-mediated iSWAP-type interactions [61]. For each gate, the participating qubits are brought into resonance through the coupler, and a parametric flux pulse is applied to acti-

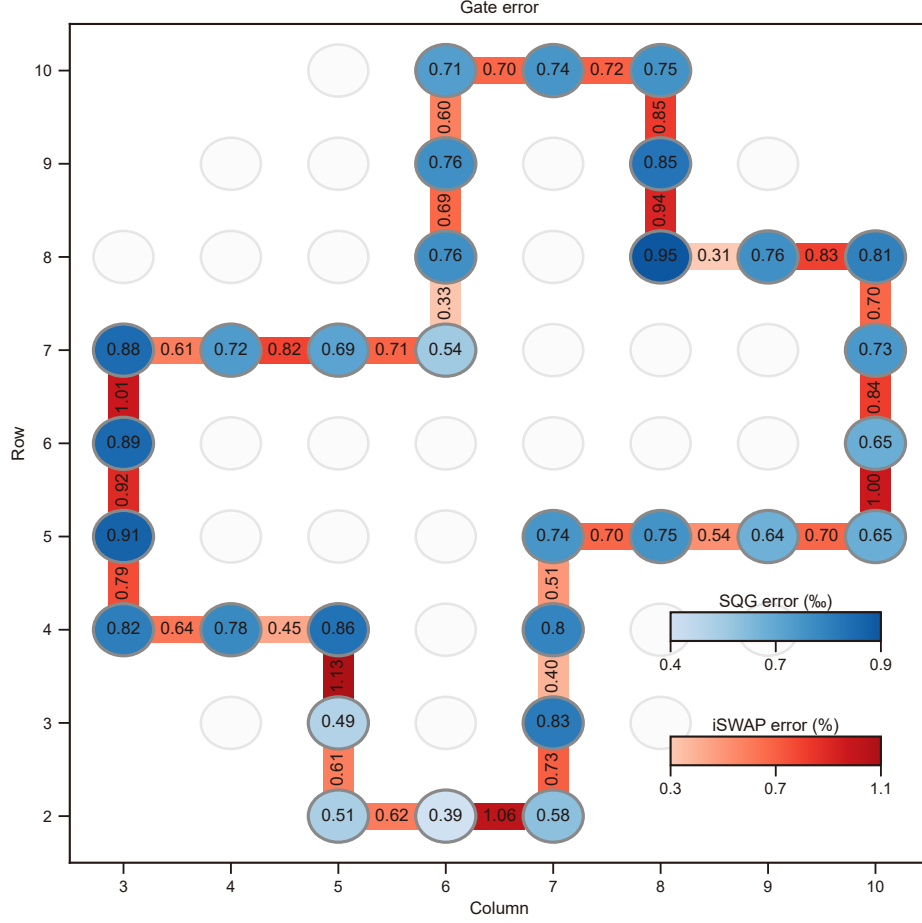


FIG. 12. **Errors of single- and two-qubit gates.** Shown are the calibrated single-qubit gate errors and the corresponding two-qubit gate errors associated with the 30 qubits used in the experiment.

vate the exchange interaction for a calibrated duration of 40 ns, corresponding to one full excitation-swap cycle at the operating point.

The gate fidelities are characterized using simultaneous benchmarking protocols. Single-qubit errors are extracted from simultaneous randomized benchmarking (RB) [62] across all 30 qubits, yielding an average error

of approximately 7×10^{-4} . Two-qubit fidelities are obtained using simultaneous speckle purity benchmarking (SPB) [63], in which odd and even couplers along the chain are benchmarked in alternating configurations to capture correlated errors. This procedure yields an average iSWAP-type gate error of about 7×10^{-3} . The calibrated single- and two-qubit gate errors used in the experiment are summarized in Fig. 12.

-
- [1] M. P. Fisher, V. Khemani, A. Nahum, and S. Vijay, Random quantum circuits, *Annual Review of Condensed Matter Physics* **14**, 335 (2023).
 - [2] A. Nahum, J. Ruhman, S. Vijay, and J. Haah, Quantum entanglement growth under random unitary dynamics, *Phys. Rev. X* **7**, 031016 (2017).
 - [3] P. Kos, B. Bertini, and T. Prosen, Exact correlation functions for dual-unitary lattice models, *Physical Review Letters* **123**, 210601 (2019).
 - [4] A. Nahum, S. Vijay, and J. Haah, Operator spreading in random unitary circuits, *Phys. Rev. X* **8**, 021014 (2018).
 - [5] C. W. von Keyserlingk, T. Rakovszky, F. Pollmann, and S. L. Sondhi, Operator hydrodynamics, otocs, and entanglement growth in systems without conservation laws, *Phys. Rev. X* **8**, 021013 (2018).
 - [6] D. A. Roberts and B. Yoshida, Chaos and complexity in quantum circuits, *Journal of High Energy Physics* **2017**, 121 (2017).
 - [7] T. Rakovszky, F. Pollmann, and C. W. von Keyserlingk, Diffusive hydrodynamics of out-of-time-ordered correlators with charge conservation, *Phys. Rev. X* **8**, 031058 (2018).

- [8] V. Khemani, A. Vishwanath, and D. A. Huse, Operator spreading and the emergence of dissipative hydrodynamics under unitary evolution with conservation laws, *Phys. Rev. X* **8**, 031057 (2018).
- [9] O. Ogunnaike, J. Feldmeier, and J. Y. Lee, Unifying emergent hydrodynamics and lindbladian low-energy spectra across symmetries, constraints, and long-range interactions, *Phys. Rev. Lett.* **131**, 220403 (2023).
- [10] M. K. Joshi, A. Elben, B. Vermersch, T. Brydges, C. Maier, P. Zoller, R. Blatt, and C. F. Roos, Quantum information scrambling in a trapped-ion quantum simulator with tunable range interactions, *Physical Review Letters* **124**, 240505 (2020).
- [11] J. Johnson, C. Macklin, D. Slichter, R. Vijay, E. Weingarten, J. Clarke, and I. Siddiqi, Heralded state preparation in a superconducting qubit, *Physical Review Letters* **109**, 050506 (2012).
- [12] X. Liang, Z. Yue, Y.-X. Chao, Z.-X. Hua, Y. Lin, M. K. Tey, and L. You, Observation of anomalous information scrambling in a rydberg atom array, *Physical Review Letters* **135**, 050201 (2025), [arXiv:2410.16174 \[quant-ph\]](#).
- [13] X. Mi, P. Roushan, C. Quintana, S. Mandrà, J. Marshall, C. Neill, *et al.*, Information scrambling in quantum circuits, *Science* **374**, 1479 (2021).
- [14] C. Ryan-Anderson, J. Bohnet, K. Lee, D. Gresh, A. Hankin, J. Gaebler, D. Francois, A. Chernoguzov, D. Lucchetti, N. Brown, T. Gatterman, S. Halit, K. Gilmore, J. Gerber, B. Neyenhuis, D. Hayes, and R. Stutz, Realization of real-time fault-tolerant quantum error correction, *Physical Review X* **11**, 041058 (2021).
- [15] S. Krinner, N. Lacroix, A. Remm, A. Di Paolo, E. Genois, C. Leroux, C. Hellings, S. Lazar, F. Swiadek, J. Hermann, *et al.*, Realizing repeated quantum error correction in a distance-three surface code, *Nature* **605**, 669 (2022).
- [16] R. Acharya, L. Aghababaie-Beni, I. Aleiner, T. I. Andersen, M. Ansmann, F. Arute, K. Arya, A. Asfaw, N. Atkhantsev, J. Atalaya, R. Babbush, D. Bacon, B. Ballard, J. C. Bardin, J. Bausch, A. Bengtsson, A. Bilmes, S. Blackwell, S. Boixo, G. Bortoli, A. Bourassa, J. Bovaird, L. Brill, M. Broughton, D. A. Browne, B. Buchea, B. B. Buckley, D. A. Buell, T. Burger, B. Burkett, N. Bushnell, A. Cabrera, J. Campero, H.-S. Chang, Y. Chen, Z. Chen, B. Chiaro, D. Chik, C. Chou, J. Claes, A. Y. Cleland, J. Cogan, R. Collins, P. Conner, W. Courtney, A. L. Crook, B. Curtin, S. Das, A. Davies, L. D. Lorenzo, D. M. Debroy, S. Demura, M. Devoret, A. D. Paolo, P. Donohoe, I. Drozdov, A. Dunsworth, C. Earle, T. Edlich, A. Eickbusch, A. M. Elbag, M. Elzouka, C. Erickson, L. Faoro, E. Farhi, V. S. Rubin, N. Saei, D. Sank, K. Sankaragomathi, K. J. Satzinger, H. F. Schurkus, C. Schuster, A. W. Senior, M. J. Shearn, A. Shorter, N. Shutty, V. Shvarts, S. Singh, V. Sivak, J. Skrzynny, S. Small, V. Smelyanskiy, W. C. Smith, R. D. Somma, S. Springer, G. Sterling, D. Strain, J. Suchard, A. Szasz, A. Sztein, D. Thor, A. Torres, M. M. Torunbalci, A. Vaishnav, J. Vargas, S. Vdovichev, G. Vidal, B. Villalonga, C. V. Heidweiller, S. Waltman, S. X. Wang, B. Ware, K. Weber, T. White, K. Wong, B. W. K. Woo, C. Xing, Z. J. Yao, P. Yeh, B. Ying, J. Yoo, N. Yosri, G. Young, A. Zalcman, Y. Zhang, N. Zhu, and N. Zobrist, Quantum error correction below the surface code threshold, *Nature* **638**, 920 (2024).
- [17] L. Caune, L. Skoric, N. S. Blunt, A. Ruban, J. McDaniel, J. A. Valery, A. D. Patterson, A. V. Gramolin, J. Majaniemi, K. M. Barnes, T. Bialas, O. Buğdaycı, O. Crawford, G. P. Gehér, H. Krovi, E. Matekole, C. Topal, S. Polletto, M. Bryant, K. Snyder, N. I. Gillespie, G. Jones, K. Johar, E. T. Campbell, and A. D. Hill, *Demonstrating real-time and low-latency quantum error correction with superconducting qubits* (2024), [arXiv:2410.05202 \[quant-ph\]](#).
- [18] B. Barber, K. M. Barnes, T. Bialas, O. Buğdaycı, E. T. Campbell, N. I. Gillespie, K. Johar, R. Rajan, A. W. Richardson, L. Skoric, C. Topal, M. L. Turner, and A. B. Ziad, A real-time, scalable, fast and resource-efficient decoder for a quantum computer, *Nature Electronics* **8**, 84 (2025).
- [19] T. Maurer, M. Bühler, M. Kröner, F. Haverkamp, T. Müller, D. Vandeth, and B. R. Johnson, *Real-time decoding of the gross code memory with fpgas* (2025), [arXiv:2510.21600 \[quant-ph\]](#).
- [20] A. Córcoles, M. Takita, K. Inoue, S. Lekuch, Z. K. Mineev, J. M. Chow, and J. M. Gambetta, Exploiting dynamic quantum circuits in a quantum algorithm with superconducting qubits, *Physical Review Letters* **127**, 100501 (2021).
- [21] M. Foss-Feig, A. Tikku, T.-C. Lu, K. Mayer, M. Iqbal, T. M. Gatterman, J. A. Gerber, K. Gilmore, D. Gresh, A. Hankin, N. Hewitt, C. V. Horst, M. Matheny, T. Mengle, B. Neyenhuis, H. Dreyer, D. Hayes, T. H. Hsieh, and I. H. Kim, *Experimental demonstration of the advantage of adaptive quantum circuits* (2023), [arXiv:2302.03029 \[quant-ph\]](#).
- [22] E. Bäumer, V. Tripathi, D. S. Wang, P. Rall, E. H. Chen, S. Majumder, A. Seif, and Z. K. Mineev, Efficient long-range entanglement using dynamic circuits, *PRX Quantum* **5**, 030339 (2024).
- [23] E. Bäumer, V. Tripathi, A. Seif, D. Lidar, and D. S. Wang, Quantum fourier transform using dynamic circuits, *Physical Review Letters* **133**, 150602 (2024).
- [24] E. Bäumer and S. Woerner, Measurement-based long-range entangling gates in constant depth, *Physical Review Research* **7**, 023120 (2025).
- [25] Y. Li, X. Chen, and M. P. A. Fisher, Quantum zeno effect and the many-body entanglement transition, *Phys. Rev. B* **98**, 205136 (2018).
- [26] Y. Li, X. Chen, and M. P. A. Fisher, Measurement-driven entanglement transition in hybrid quantum circuits, *Phys. Rev. B* **100**, 134306 (2019).
- [27] B. Skinner, J. Ruhman, and A. Nahum, Measurement-induced phase transitions in the dynamics of entanglement, *Phys. Rev. X* **9**, 031009 (2019).
- [28] A. Chan, R. M. Nandkishore, M. Pretko, and G. Smith, Unitary-projective entanglement dynamics, *Phys. Rev. B* **99**, 224307 (2019).
- [29] C.-M. Jian, Y.-Z. You, R. Vasseur, and A. W. W. Ludwig, Measurement-induced criticality in random quantum circuits, *Phys. Rev. B* **101**, 104302 (2020).
- [30] M. J. Gullans and D. A. Huse, Dynamical purification phase transition induced by quantum measurements, *Physical Review X* **10**, 041020 (2020).
- [31] C. Noel, P. Niroula, D. Zhu, A. Risinger, L. Egan, D. Biswas, M. Cetina, A. V. Gorshkov, M. J. Gullans, D. A. Huse, *et al.*, Measurement-induced quantum phases realized in a trapped-ion quantum computer, *Nature Physics* **18**, 760 (2022).
- [32] J. M. Koh, S.-N. Sun, M. Motta, and A. J. Minnich,

- Measurement-induced entanglement phase transition on a superconducting quantum processor with mid-circuit readout, *Nature Physics* **19**, 1314 (2023).
- [33] J. C. Hoke, M. Ippoliti, E. Rosenberg, D. Abanin, R. Acharya, T. I. Andersen, M. Ansmann, F. Arute, K. Arya, A. Asfaw, J. Atalaya, J. C. Bardin, A. Bengtsson, G. Bortoli, A. Bourassa, J. Bovaird, L. Brill, M. Broughton, B. B. Buckley, D. A. Buell, T. Burger, B. Burkett, N. Bushnell, Z. Chen, B. Chiaro, D. Chik, J. Cogan, R. Collins, P. Conner, W. Courtney, A. L. Crook, B. Curtin, A. G. Dau, D. M. Debroy, A. Del Toro Barba, S. Demura, A. Di Paolo, I. K. Drozdov, A. Dunsworth, D. Eppens, C. Erickson, E. Farhi, R. Fatemi, V. S. Ferreira, L. F. Burgos, E. Forati, A. G. Fowler, B. Foxen, W. Giang, C. Gidney, D. Gilboa, M. Giustina, R. Gosula, J. A. Gross, S. Habegger, M. C. Hamilton, M. Hansen, M. P. Harrigan, S. D. Harrington, P. Heu, M. R. Hoffmann, S. Hong, T. Huang, A. Huff, W. J. Huggins, S. V. Isakov, J. Iveland, E. Jeffrey, Z. Jiang, C. Jones, P. Juhas, D. Kafri, K. Kechedzhi, T. Khattar, M. Khezri, M. Kieferovaj, S. Kim, A. Kitaev, P. V. Klimov, A. R. Klots, A. N. Korotkov, F. Kostritsa, J. M. Kreikebaum, D. Landhuis, P. Laptev, K.-M. Lau, L. Laws, J. Lee, K. W. Lee, Y. D. Lensky, B. J. Lester, A. T. Lill, W. Liu, A. Locharla, O. Martin, J. R. McClean, M. McEwen, K. C. Miao, A. Mieszala, S. Montazeri, A. Morvan, R. Movassagh, W. Mruczkiewicz, M. Neeley, C. Neill, A. Nersisyan, M. Newman, J. H. Ng, A. Nguyen, M. Nguyen, M. Y. Niu, T. E. OaBrien, S. Omonije, A. Opremcak, A. Petukhov, R. Potter, L. P. Pryadko, C. Quintana, C. Rocque, N. C. Rubin, N. Saei, D. Sank, K. Sankaragomathi, K. J. Satzinger, H. F. Schurkus, C. Schuster, M. J. Shearn, A. Shorter, N. Shutty, V. Shvarts, J. Skrzyny, W. C. Smith, R. Somma, G. Sterling, D. Strain, M. Szalay, A. Torres, G. Vidal, B. Villalonga, C. V. Heidweiller, T. White, B. W. K. Woo, C. Xing, Z. J. Yao, P. Yeh, J. Yoo, G. Young, A. Zalcman, Y. Zhang, N. Zhu, N. Zobrist, H. Neven, R. Babbush, D. Bacon, S. Boixo, J. Hilton, E. Lucero, A. Megrant, J. Kelly, Y. Chen, V. Smelyanskiy, X. Mi, V. Khemani, and P. Roushan, Measurement-induced entanglement and teleportation on a noisy quantum processor, *Nature* **622**, 481 (2023).
- [34] T. Iadecola, S. Ganesan, J. H. Pixley, and J. H. Wilson, Measurement and feedback driven entanglement transition in the probabilistic control of chaos, *Phys. Rev. Lett.* **131**, 060403 (2023).
- [35] V. Ravindranath, Y. Han, Z.-C. Yang, and X. Chen, Entanglement steering in adaptive circuits with feedback, *Phys. Rev. B* **108**, L041103 (2023).
- [36] N. O’Dea, A. Morningstar, S. Gopalakrishnan, and V. Khemani, Entanglement and absorbing-state transitions in interactive quantum dynamics, *Phys. Rev. B* **109**, L020304 (2024).
- [37] L. Piroli, Y. Li, R. Vasseur, and A. Nahum, Triviality of quantum trajectories close to a directed percolation transition, *Phys. Rev. B* **107**, 224303 (2023).
- [38] P. Sierant and X. Turkeshi, Controlling entanglement at absorbing state phase transitions in random circuits, *Phys. Rev. Lett.* **130**, 120402 (2023).
- [39] V. Ravindranath, Z.-C. Yang, and X. Chen, Free fermions under adaptive quantum dynamics, *Quantum* **9**, 1685 (2025).
- [40] S. Morales, Y. Gefen, I. Gornyi, A. Zazunov, and R. Egger, Engineering unsteerable quantum states with active feedback, *Physical Review Research* **6**, 013244 (2024).
- [41] J. Hauser, Y. Li, S. Vijay, and M. P. A. Fisher, Continuous symmetry breaking in adaptive quantum dynamics, *Physical Review B* **109**, 214305 (2024).
- [42] A. A. Allocca, C. LeMaire, T. Iadecola, and J. H. Wilson, Statistical mechanics of stochastic quantum control: d -adic renyi circuits, *Physical Review E* **110**, 024113 (2024).
- [43] B. Pokharel, H. Pan, K. Aziz, L. C. G. Govia, S. Ganesan, T. Iadecola, J. H. Wilson, B. A. Jones, A. Deshpande, J. H. Pixley, and M. Takita, *Order from chaos with adaptive circuits on quantum hardware* (2025), [arXiv:2509.18259 \[quant-ph\]](https://arxiv.org/abs/2509.18259).
- [44] M. Foss-Feig, A. Tikku, T.-C. Lu, K. Mayer, M. Iqbal, T. M. Gatterman, J. A. Gerber, K. Gilmore, D. Gresh, A. Hankin, N. Hewitt, C. V. Horst, M. Matheny, T. Mengle, B. Neyenhuis, H. Dreyer, D. Hayes, T. H. Hsieh, and I. H. Kim, *Experimental demonstration of the advantage of adaptive quantum circuits* (2023), [arXiv:2302.03029 \[quant-ph\]](https://arxiv.org/abs/2302.03029).
- [45] T.-C. Lu, L. A. Lessa, I. H. Kim, and T. H. Hsieh, Measurement as a shortcut to long-range entangled quantum matter, *PRX Quantum* **3**, 040337 (2022).
- [46] E. Chertkov, Z. Cheng, A. C. Potter, S. Gopalakrishnan, T. M. Gatterman, J. A. Gerber, K. Gilmore, D. Gresh, A. Hall, A. Hankin, M. Matheny, T. Mengle, D. Hayes, B. Neyenhuis, R. Stutz, and M. Foss-Feig, Characterizing a non-equilibrium phase transition on a quantum computer, *Nature Physics* **19**, 1799 (2023).
- [47] W. Huang, X.-C. Zhou, L. Zhang, J. Zhang, Y. Zhou, Z. Guo, B.-C. Yao, P. Huang, Q. Li, Y. Liang, *et al.*, Exact quantum critical states with a superconducting quantum processor, *arXiv preprint arXiv:2502.19185* (2025).
- [48] M. Henkel, H. Hinrichsen, and S. Lubeck, *Non-Equilibrium Phase Transitions: Volume I: Absorbing Phase Transitions* (Springer, 2008).
- [49] Z. Chen, K. J. Satzinger, J. Atalaya, A. N. Korotkov, A. Dunsworth, D. Sank, C. Quintana, M. McEwen, R.arends, P. V. Klimov, S. Hong, C. Jones, A. Petukhov, D. Kafri, S. Demura, B. Burkett, C. Gidney, A. G. Fowler, A. Paler, H. Putterman, I. Aleiner, F. Arute, K. Arya, R. Babbush, J. C. Bardin, A. Bengtsson, A. Bourassa, M. Broughton, B. B. Buckley, D. A. Buell, N. Bushnell, B. Chiaro, R. Collins, W. Courtney, A. R. Derk, D. Eppens, C. Erickson, E. Farhi, B. Foxen, M. Giustina, A. Greene, J. A. Gross, M. P. Harrigan, S. D. Harrington, J. Hilton, A. Ho, T. Huang, W. J. Huggins, L. B. Ioffe, S. V. Isakov, E. Jeffrey, Z. Jiang, K. Kechedzhi, S. Kim, A. Kitaev, F. Kostritsa, D. Landhuis, P. Laptev, E. Lucero, O. Martin, J. R. McClean, T. McCourt, X. Mi, K. C. Miao, M. Mohseni, S. Montazeri, W. Mruczkiewicz, J. Mutus, O. Naaman, M. Neeley, C. Neill, M. Newman, M. Y. Niu, T. E. O’Brien, A. Opremcak, E. Ostby, B. Pato, N. Redd, P. Roushan, N. C. Rubin, V. Shvarts, D. Strain, M. Szalay, M. D. Trevithick, B. Villalonga, T. White, Z. J. Yao, P. Yeh, J. Yoo, A. Zalcman, H. Neven, S. Boixo, V. Smelyanskiy, Y. Chen, A. Megrant, and J. Kelly, Exponential suppression of bit or phase errors with cyclic error correction, *Nature* **595**, 383 (2021).
- [50] J. Bylander, S. Gustavsson, F. Yan, F. Yoshihara, K. Harrabi, G. Fitch, D. G. Cory, Y. Nakamura, J.-S. Tsai, and W. D. Oliver, Noise spectroscopy through dy-

- namical decoupling with a superconducting flux qubit, *Nature Physics* **7**, 565 (2011).
- [51] M. Szyniszewski, A. Romito, and H. Schomerus, Entanglement transition from variable-strength weak measurements, *Phys. Rev. B* **100**, 064204 (2019).
 - [52] M. Christandl and R. Renner, Reliable quantum state tomography, *Physical Review Letters* **109**, 120403 (2012).
 - [53] X. Yang, J. Chu, Z. Guo, W. Huang, Y. Liang, J. Liu, J. Qiu, X. Sun, Z. Tao, J. Zhang, *et al.*, Coupler-assisted leakage reduction for scalable quantum error correction with superconducting qubits, *Physical Review Letters* **133**, 170601 (2024).
 - [54] F. B. Maciejewski, Z. Zimborás, and M. Oszmaniec, Mitigation of readout noise in near-term quantum devices by classical post-processing based on detector tomography, *Quantum* **4**, 257 (2020).
 - [55] B. Nachman, M. Urbanek, W. A. de Jong, and C. W. Bauer, Unfolding quantum computer readout noise, *npj Quantum Information* **6**, 10.1038/s41534-020-00309-7 (2020).
 - [56] J. Zhang, X. Sun, Z. Guo, Y. Yuan, Y. Zhang, J. Chu, W. Huang, Y. Liang, J. Qiu, D. Sun, Z. Tao, J. Zhang, W. Guo, J. Jiang, X. Linpeng, Y. Liu, W. Ren, J. Niu, Y. Zhong, and D. Yu, M² CS: A microwave measurement and control system for large-scale superconducting quantum processors, *Chin. Phys. B* **33**, 120309 (2024).
 - [57] X. Sun, L. Li, Z. Wu, Z. Guo, P. Huang, W. Huang, Q. Li, Y. Liang, Y. Liu, D. Sun, Z. Wang, C. Xie, Y. Xiong, X. Yang, J. Zhang, J. Zhang, L. Zhang, Z. Zhang, W. Guo, J. Jiang, S. Liu, X. Linpeng, J. Niu, J. Qiu, W. Ren, Z. Tao, Y. Yuan, Y. Zhou, J. Chu, Y. Zhong, X. Sun, and D. Yu, Logical operations with a dynamical qubit in floquet-bacon-shor code, *Physical Review Letters* **135**, 10.1103/425n-6k9s (2025).
 - [58] J. Heinsoo, C. K. Andersen, A. Remm, S. Krinner, T. Walter, Y. Salathé, S. Gasparinetti, J.-C. Besse, A. Potočník, A. Wallraff, and C. Eichler, Rapid high-fidelity multiplexed readout of superconducting qubits, *Phys. Rev. Appl.* **10**, 034040 (2018).
 - [59] F. Motzoi, J. M. Gambetta, P. Rebentrost, and F. K. Wilhelm, Simple pulses for elimination of leakage in weakly nonlinear qubits, *Physical Review Letters* **103**, 110501 (2009).
 - [60] J. M. Chow, L. DiCarlo, J. M. Gambetta, F. Motzoi, L. Frunzio, S. M. Girvin, and R. J. Schoelkopf, Optimized driving of superconducting artificial atoms for improved single-qubit gates, *Physical Review A* **82**, 040305 (2010).
 - [61] Y. Sung, L. Ding, J. Braumüller, A. Vepsäläinen, B. Kannan, M. Kjaergaard, A. Greene, G. O. Samach, C. McNally, D. Kim, A. Melville, B. M. Niedzielski, M. E. Schwartz, J. L. Yoder, T. P. Orlando, S. Gustavsson, and W. D. Oliver, Realization of high-fidelity *cz* and *zz*-free *iswap* gates with a tunable coupler, *Phys. Rev. X* **11**, 021058 (2021).
 - [62] J. Emerson, R. Alicki, and K. Życzkowski, Scalable noise estimation with random unitary operators, *Journal of Optics B: Quantum and Semiclassical Optics* **7**, S347 (2005).
 - [63] F. Arute, K. Arya, R. Babbush, D. Bacon, J. C. Bardin, R. Barends, R. Biswas, S. Boixo, F. G. Brandao, D. A. Buell, *et al.*, Quantum supremacy using a programmable superconducting processor, *Nature* **574**, 505 (2019).